# Collinear Three-Photon Excitation of a Strongly Forbidden Optical Clock Transition

Samuel P. Carman , <sup>1</sup>, \* Jan Rudolph , <sup>1</sup>, <sup>2</sup>, \* Benjamin E. Garber , <sup>1</sup>, \* Michael J. Van de Graaff , <sup>1</sup> Hunter Swan , <sup>1</sup> Yijun Jiang (姜一君) , <sup>3</sup> Megan Nantel , <sup>3</sup> Mahiro Abe , <sup>1</sup> Rachel L. Barcklay , <sup>4</sup> and Jason M. Hogan , <sup>1</sup>

<sup>1</sup>Department of Physics, Stanford University, Stanford, California 94305, USA

<sup>2</sup>Fermi National Accelerator Laboratory, Batavia, Illinois 60510, USA

<sup>3</sup>Department of Applied Physics, Stanford University, Stanford, California 94305, USA

<sup>4</sup>Department of Electrical Engineering, Stanford University, Stanford, California 94305, USA

(Dated: August 27, 2025)

The  $^1\mathrm{S}_0-^3\mathrm{P}_0$  clock transition in strontium serves as the foundation for the world's best atomic clocks and for gravitational wave detector concepts in clock atom interferometry. This transition is weakly allowed in the fermionic isotope  $^{87}\mathrm{Sr}$  but strongly forbidden in bosonic isotopes. Here, we demonstrate coherent excitation of the clock transition in bosonic  $^{88}\mathrm{Sr}$  using a novel collinear three-photon process in a weak magnetic field. We observe Rabi oscillations with frequencies of up to 50 kHz using W/cm² laser intensities and Gauss-level magnetic field amplitudes. The absence of nuclear spin in bosonic isotopes offers decreased sensitivity to magnetic fields and optical lattice light shifts, enabling atomic clocks with reduced systematic errors. The collinear propagation of the laser fields permits the interrogation of spatially separated atomic ensembles with common laser pulses, a key requirement for dark matter searches and gravitational wave detection with next-generation quantum sensors.

Narrow optical transitions to long-lived atomic states are essential for many applications in metrology [1–3], precision timekeeping [4–6], and tests of fundamental physics [7–10]. The most accurate optical atomic clocks use  ${}^{1}S_{0} - {}^{3}P_{0}$  singletto-triplet transitions in alkaline-earth-like neutral atoms and ions (e.g. Sr, Yb, Mg, Al<sup>+</sup>) [11–14]. These ultranarrow transitions are weakly allowed in fermions because of the hyperfine interaction, but are strongly forbidden in bosons, where a large external magnetic field is required to induce a comparable coupling strength [15–18]. Bosonic isotopes of neutral atoms promise considerable advantages, such as their lack of nuclear spin, simplified laser cooling and state preparation, as well as the scalar polarizability of their clock states [5, 19]. To access these desirable properties, coherent multiphoton processes in bosons have been proposed [19–22]. Of particular interest is the three-photon excitation  $^1\mathrm{S}_0 \to$  $^{3}P_{1} \rightarrow ^{3}S_{1} \rightarrow ^{3}P_{0}$  [20, 23], using a set of laser frequencies readily available for laser cooling, repumping, and imaging.

Ostensibly, this coherent three-photon excitation cannot be driven with collinear laser beams due to angular momentum selection rules [21, 24]. Instead, at least one of the beams must be sent from a different direction. This is easily accommodated in most clock applications, where the beams can even be arranged to eliminate the net momentum transfer to the atoms [23,25]. In contrast, collinear laser beams are advantageous in applications where several atomic ensembles are ideally addressed with identical laser pulses, such as multiqubit entanglement in optical tweezer arrays [26–29], differential operation of atomic clocks [30–35], and gradiometer configurations in clock atom interferometry [36, 37]. In gradiometers, common laser pulses are particularly important for laser frequency noise suppression, which requires that all spectral content must be delivered from the same direction [38]. Like clocks, clock atom interferometry proposals generally rely on naturally occurring narrow-line transitions in fermions [37]. Because of the weak coupling, interferometry pulses on these transitions are slow and the interferometer sensitivity is ultimately limited by the number of pulses that can be applied. Unlocking bosonic isotopes for long-baseline clock atom interferometry via multiphoton processes could lead to a substantial increase in sensitivity by engineering an effective transition with both strong coupling and long excited state lifetime.

Here, we demonstrate a coherent, collinear three-photon process  ${}^{1}S_{0} \rightarrow {}^{3}P_{1} \rightarrow {}^{3}S_{1} \rightarrow {}^{3}P_{0}$  in bosonic  ${}^{88}Sr$  mediated by a weak magnetic bias field. The constant field lifts the degeneracy of the intermediate <sup>3</sup>P<sub>1</sub> sublevels that otherwise leads to destructive interference of the excitation paths. We show why this transition cannot be driven with collinear laser beams without a magnetic field and illustrate the transformation of the effective angular wave function of <sup>3</sup>P<sub>1</sub> under the associated external torque. We drive this three-photon transition using a single trichromatic laser pulse, delivered via a polarization-maintaining optical fiber. We observe Rabi oscillations between the clock states <sup>1</sup>S<sub>0</sub> and <sup>3</sup>P<sub>0</sub> with frequencies of up to 50 kHz, substantially surpassing what could be achieved with similar laser intensities on the naturally occurring single-photon transition in fermionic <sup>87</sup>Sr and the magnetic-field-induced transition in <sup>88</sup>Sr.

With this new technique, we demonstrate the first multiphoton clock atom interferometer using a Mach-Zehnder pulse sequence. Since all spectral content for the three-photon transition is copropagating, this interferometer scheme is compatible with long-baseline clock gradiometers like MAGIS-100 [37]. Bosonic isotopes can now be employed in such experiments, which extends the utility of next-generation quantum sensors.

Alkaline-earth-like atoms such as strontium have two valence electrons and their atomic states are split into a singlet and a triplet manifold [see Fig. 1(a)]. While strong electric dipole transitions are possible within each manifold, spin-flipping electric dipole transitions between singlet and triplet states are generally forbidden. A notable exception is the

<sup>\*</sup> These authors contributed equally to this work.

<sup>†</sup> hogan@stanford.edu

 $^{1}\mathrm{S}_{0} - ^{3}\mathrm{P}_{1}$  transition, which is weakly allowed through spinorbit coupling. The three-photon process described here combines this weak intercombination line and two strong electric dipole transitions into one coherent excitation.

The coupling strength of this multiphoton transition can be expressed as the product of the individual single-photon couplings  $\Omega_i$  divided by the intermediate laser frequency detunings  $\Delta_i$  [Fig. 1(b)]. When using linearly polarized light fields, the effective three-photon coupling can be written as

$$\Omega_{\text{eff}} = \frac{\Omega_1 \Omega_2 \Omega_3}{2\Delta_2} \, \epsilon_{jkl} \, D_{jn} \, e_n^{(1)} e_k^{(2)} e_l^{(3)}, \tag{1}$$

where  $\epsilon_{jkl}$  is the Levi-Civita symbol, and  $e_n^{(i)}$  is the  $n^{\text{th}}$  Cartesian component of the  $i^{\text{th}}$  laser's polarization vector, with an implicit sum over repeated indices (see Appendix D 5). The entries of the matrix  $D_{jn}$  depend on the inverse detunings  $1/\Delta_{1,m}$  to the three magnetic sublevels m of  ${}^3\mathrm{P}_1$ . When these sublevels are degenerate,  $D_{jn}=\frac{1}{\Delta_1}\delta_{jn}$  is diagonal and Eq.(1) reduces to

$$\Omega_{\text{eff}} = \frac{\Omega_1 \Omega_2 \Omega_3}{2\Delta_1 \Delta_2} \ \mathbf{e}^{(1)} \cdot \left( \mathbf{e}^{(2)} \times \mathbf{e}^{(3)} \right). \tag{2}$$

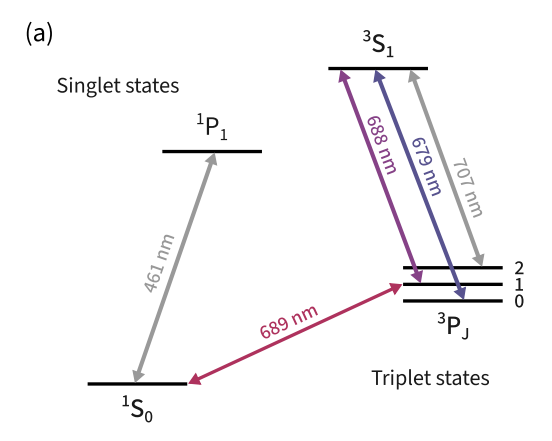
The three-photon coupling therefore scales with the volume spanned by the electric field polarization vectors, which vanishes for collinearly propagating optical fields.

Applying an external magnetic field **B** along  $\hat{\mathbf{z}}$  lifts the degeneracy of the  ${}^3\mathrm{P}_1$  sublevels via a Zeeman shift  $\delta\omega_B=g_J\,\mu_\mathrm{B}\,B/\hbar$ , where  $g_J$  is the Landé g factor and  $\mu_\mathrm{B}$  is the Bohr magneton [see Fig. 1(b)]. Choosing a set of polarizations  $\mathbf{e}^{(1)}=\mathbf{e}^{(2)}=\hat{\mathbf{x}}$  and  $\mathbf{e}^{(3)}=\hat{\mathbf{z}}$  with collinear propagation direction  $\hat{\mathbf{y}}$ , the coupling becomes

$$\Omega_{\text{eff}} = \frac{\Omega_1 \Omega_2 \Omega_3}{4\Delta_2} \left( \frac{1}{\Delta_1 - \delta\omega_B} - \frac{1}{\Delta_1 + \delta\omega_B} \right).$$
 (3)

The minus sign between the terms conveys the destructive interference of the two excitation paths (via m=-1 and m=+1) in the absence of a magnetic field.

The optical field requirements without external magnetic field can be illustrated using the angular part of the atomic wave function, which consists of an entangled superposition of orbital angular momentum L and spin angular momentum **S** [see Fig. 2(a)]. The light field at 689 nm along  $\hat{\mathbf{x}}$  drives a weakly allowed singlet-to-triplet transition to <sup>3</sup>P<sub>1</sub> possible only through spin-orbit coupling. The triplet component of the resulting state has the form  $(|L_y\rangle |S_z\rangle - |L_z\rangle |S_y\rangle)$ , where  $|L_n\rangle$  and  $|S_n\rangle$  are the Cartesian basis states of the orbital angular momentum and spin operators (see Appendix D 2). Here, the symmetry axes of these p orbitals  $|L_n\rangle$  are orthogonal to the polarization of the exciting laser. In contrast, the other two light fields at 688 and 679 nm drive spin-preserving, dipoleallowed transitions where the polarization of the light has to match the p orbital symmetry axis of the associated spin projection  $|S_n\rangle$  (color). Since the final state of the three-photon process  ${}^{3}P_{0}$  has the form  $(|L_{x}\rangle |S_{x}\rangle + |L_{y}\rangle |S_{y}\rangle + |L_{z}\rangle |S_{z}\rangle)$ , two mutually orthogonal polarization components are required to reach the appropriate spin state (either via the green path



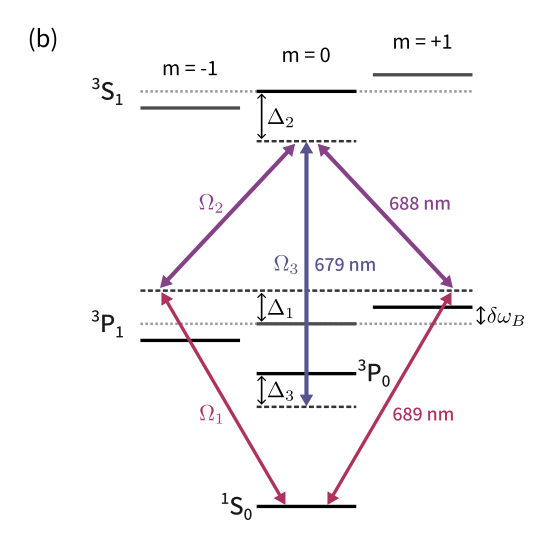


FIG. 1. (a) Singlet and triplet states of  $^{88}\mathrm{Sr}$  and the relevant transition wavelength connecting the atomic states. We describe a three-photon transition between  $^1\mathrm{S}_0$  and  $^3\mathrm{P}_0$  using laser light at 689 nm (magenta), 688 nm (purple), and 679 nm (blue). (b) Energy levels involved in the three-photon transition with Zeeman sublevels m in the presence of a magnetic field, causing a relative shift  $\delta\omega_B$ . The polarizations of the optical fields are linear, with 689 nm  $(\Omega_1)$  and 688 nm  $(\Omega_2)$  normal, and 679 nm  $(\Omega_3)$  parallel to the quantization axis. Cumulative frequency detunings of the lasers from the respective m=0 states are denoted by  $\Delta_1,\,\Delta_2,\,\mathrm{and}\,\Delta_3.$ 

or the blue path). Thus, Fig. 2(a) is a visual representation of the scalar triple product in Eq. (2), illustrating the need for noncopropagating light fields [39].

Applying a magnetic field along  $\hat{\mathbf{z}}$  alters the angular part of the effective  $^3P_1$  wave function

$$|^{3}P_{1}, \theta_{B}\rangle = \frac{1}{\sqrt{2}} \left( \sin \theta_{B} |L_{x}\rangle + i \cos \theta_{B} |L_{y}\rangle \right) |S_{z}\rangle - \frac{1}{\sqrt{2}} |L_{z}\rangle \left( \sin \theta_{B} |S_{x}\rangle + i \cos \theta_{B} |S_{y}\rangle \right),$$
(4)

where we define the angle  $\theta_B \equiv \arctan \beta$ , with dimensionless ratio  $\beta \equiv \delta \omega_B/\Delta_1$ . With increasing  $\theta_B$  the state acquires both a spin and an orbital angular momentum component along  $\hat{\mathbf{x}}$ . The three-photon transition can now be driven with collinear laser beams, e.g. using  $\hat{\mathbf{x}} - \hat{\mathbf{x}} - \hat{\mathbf{z}}$  polarizations [see Fig. 2(b)].

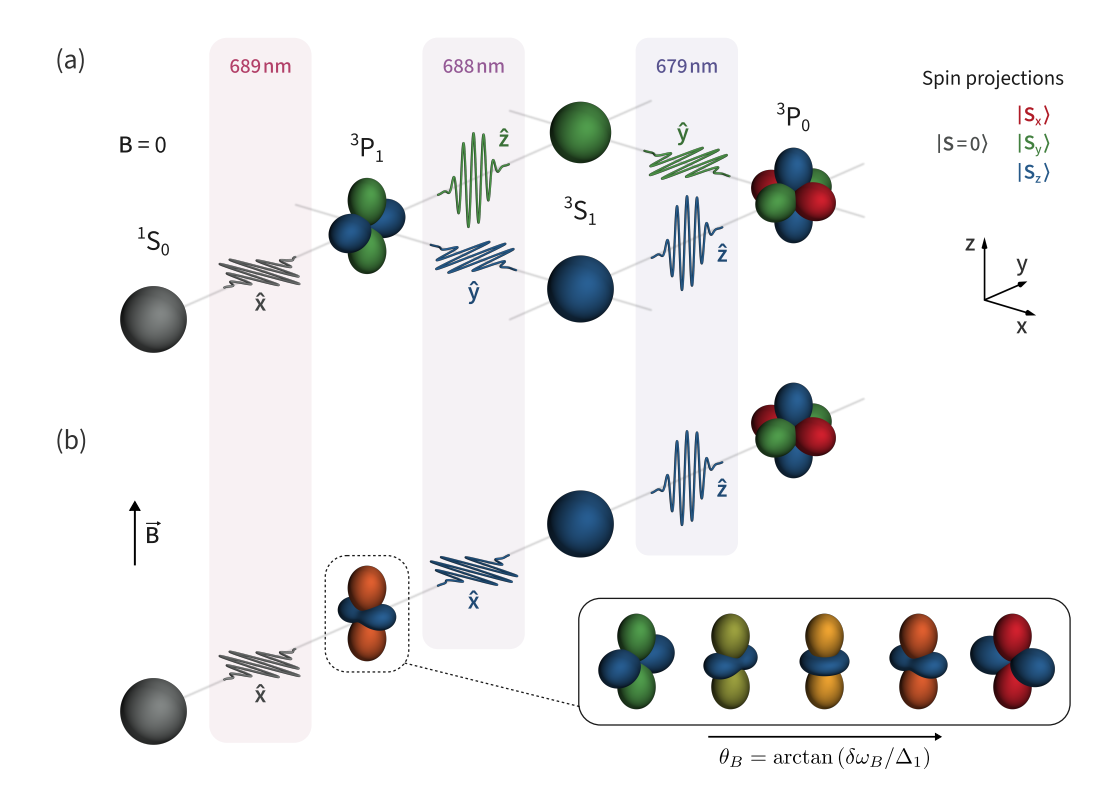


FIG. 2. Engineering a collinear three-photon transition. Cartesian basis representation of the orbital angular momentum (shape) and spin (color) of the atomic wave function during the three-photon transition  ${}^1S_0 \rightarrow {}^3P_1 \rightarrow {}^3P_1 \rightarrow {}^3P_0$ . While we depict the three-photon process as a sequence of interactions, the coherent excitation is nonsequential and all fields are applied simultaneously. The light fields linking the states are shown with the required polarizations, and spin-preserving transitions (688 and 679 nm) are colored according to the spin state  $|S_x\rangle$  (red),  $|S_y\rangle$  (green), and  $|S_z\rangle$  (blue). (a) Contrary to the dipole-allowed transitions, the light at 689 nm causes an excitation orthogonal to its polarization along  $\hat{\bf x}$  and changes the spin state. The other two transitions are spin- (color) preserving and the light polarizations need to be aligned with the respective p orbitals. To reach the appropriate spin projection of  ${}^3P_0$  via either the  $\hat{\bf x} - \hat{\bf y} - \hat{\bf z}$  (blue) or  $\hat{\bf x} - \hat{\bf z} - \hat{\bf y}$  (green) combination, at least one of the polarization vectors must have a noncoplanar component with respect to the other two. (b) Applying a magnetic field along  $\hat{\bf z}$  deforms the effective angular wave function of  ${}^3P_1$  and permits driving the three-photon transition with collinear light via  $\hat{\bf x} - \hat{\bf x} - \hat{\bf z}$  (blue). Inset: the effective wave function for various angles  $\theta_B$  from 0° to 90° (maximal projection along  $\hat{\bf x}$ ). Note that the collinear combination  $\hat{\bf x} - \hat{\bf z} - \hat{\bf x}$  (red) would now also be permitted (not shown).

We demonstrate this coherent three-photon excitation using a thermal ensemble of bosonic  $^{88}$ Sr atoms. In a constant magnetic field aligned with  $\hat{\mathbf{z}}$ , a single laser pulse containing all three wavelengths is applied to the atoms along the  $\hat{\mathbf{y}}$  direction. The laser light at 689 and 688 nm is linearly polarized along  $\hat{\mathbf{x}}$ , while the 679 nm component is linearly polarized along  $\hat{\mathbf{z}}$ . To avoid populating any of the intermediate states, the lasers are each detuned from their respective single-photon resonance by several hundred natural linewidths using an optical frequency comb as a reference. To estimate the three-photon pulse fidelity, we measure the populations in the ground state  $^{1}$ S<sub>0</sub> and in all metastable exited states  $^{3}$ P<sub>J</sub> using a state-selective imaging scheme (see Appendix A 2).

The resonance frequency for the three-photon transition is given by the effective detuning  $\Delta_{\text{eff}} \equiv \Delta_3 + \Omega_{\text{ac}}$ , with cumulative laser detuning  $\Delta_3$  and ac-Stark shift (see Appendix C 1):

$$\Omega_{\rm ac} = -\frac{\Omega_1^2}{2} \frac{\Delta_1}{\Delta_1^2 - \delta\omega_B^2} + \frac{\Omega_3^2}{4\Delta_2}.$$
 (5)

We vary the laser detuning  $\Delta_3$  around the calculated resonance frequency and find the three-photon transition as expected.

Figure 3(a) shows such a line scan with peak excited state transfer of 32% and a line shape that fits to a Voigt profile with HWHM of 57(6) kHz. At the measured three-photon resonance, we scan the pulse duration and observe Rabi oscillations in the  ${}^{3}P_{0}$  population with a fitted frequency of 30.2(2) kHz [see Fig. 3(b)]. This is in good agreement with the predicted three-photon Rabi frequency of 28(1) kHz from Eq. (3), using laser intensities  $(I_1, I_2, I_3) = (0.16, 1.4, 0.91)$  W/cm<sup>2</sup> and a magnetic field amplitude of 10.1 G (see Appendix A). The low state transfer and noticeable damping of the Rabi oscillation stem from the temperature of the atoms, laser frequency noise, and intensity inhomogeneity across the cloud, since we intentionally focus the laser beam to increase the peak intensity. Much of this damping can be avoided simply by using a larger beam size (see Appendix B). The populations in the other metastable excited states  ${}^3P_1$  and  ${}^3P_2$  are small, consistent with minimal off-resonant single-photon excitation.

We compare the observed three-photon dynamics to a density matrix simulation that includes all dipole-allowed couplings and decay channels between the 13 magnetic sublevels of the  $^{1}\mathrm{S}_{0}$ ,  $^{3}\mathrm{S}_{1}$ , and  $^{3}\mathrm{P}_{J}$  states. For each state population,

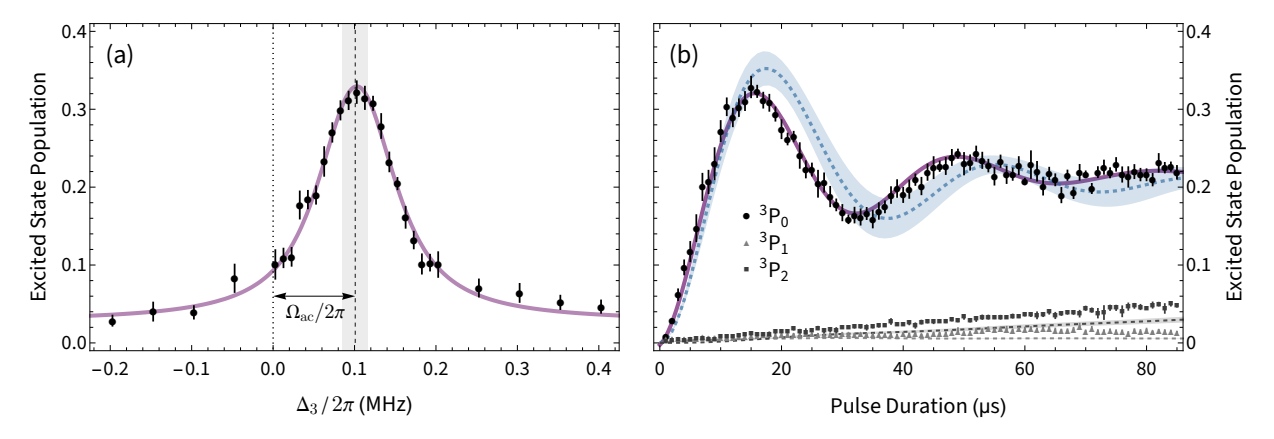


FIG. 3. Coherent three-photon excitation of the  $^1S_0-^3P_0$  clock transition. (a) Line scan of the three-photon transition showing the fractional excited state population versus the cumulative laser detuning  $\Delta_3$ , using  $\Delta_1/2\pi=9.95(1)$  MHz,  $\Delta_2/2\pi=-2.54$  GHz, and  $\delta\omega_B/2\pi=21.13(1)$  MHz. Each data point is an average of five measurements and the error bars represent the standard error of the mean. The location of  $\Delta_3=0$  is a prediction based on the measured absolute frequencies of the lasers and the literature values for the strontium transition energies. The dashed line and shaded region indicate the expected resonance location at  $\Delta_{\rm eff}=0$  and its uncertainty, with a calculated ac-Stark shift of  $\Omega_{\rm ac}/2\pi=-101(16)$  kHz from Eq. (5). This agrees well with the Voigt profile fit to the data (solid curve), from which we extract a center frequency of 103(1) kHz. (b) Rabi oscillation at the measured three-photon resonance frequency, showing the fractional excited state populations versus the pulse duration. Circles, triangles, and squares indicate the population in the states  $^3P_0$ ,  $^3P_1$ , and  $^3P_2$ , respectively. Each data point is an average of five measurements and the error bars represent the standard error of the mean. The dashed curves (blue, dark gray, light gray) correspond to the time traces predicted by the density matrix simulation averaged over the measured broadening, and the bands are the  $\pm 1\sigma$  predictions based on the uncertainties in the simulation parameters. The solid curve (purple) is a fit to an exponentially damped sinusoid used to extract the observed Rabi frequency of 30.2(2) kHz.

we compute a weighted average that accounts for Doppler shifts, laser frequency noise, and intensity inhomogeneity. In Figure 3(b), we show the predicted populations as a function of time, using the measured cloud size and temperature, laser beam size, and cumulative laser frequency noise. This parameter-free model qualitatively agrees with the experimentally observed dynamics, which feature a slightly larger damping rate of the Rabi oscillation as well as larger residual populations in the other triplet states. We attribute these deviations in part to the simplified laser noise model which assumes a Gaussian distribution for the atom-laser detuning. Other factors include inhomogeneity of the imaging beam intensity and residual crosstalk between the image measurement ports (see Appendix A 2). The majority of the damping (97%) is explained by the temperature of the atoms, the laser beam size, and laser noise. Off-resonant scattering inherent to the three-photon process accounts for only a small portion of the damping (3%). We summarize the individual contributions to the damping rate of the modeled three-photon Rabi oscillation in Table II. Our density matrix simulation shows that this loss can be reduced further with an appropriate choice of laser intensities and detunings to support a state transfer of over 99% while maintaining a Rabi frequency of at least 10 kHz (see Appendix B).

We further characterize the three-photon process at various magnetic fields and laser detunings by measuring the resonant Rabi frequencies and comparing their magnitudes. It is convenient to parametrize the coupling via the ratio of the detunings  $\beta=\delta\omega_B/\Delta_1$  such that Eq. (3) can be written as

$$\Omega_{\text{eff}} = \Omega_0 \, \frac{\beta}{1 - \beta^2},\tag{6}$$

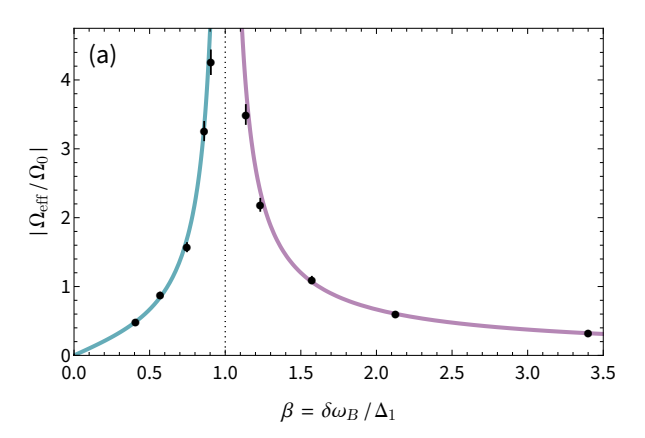
where  $\Omega_0 \equiv \Omega_1\Omega_2\Omega_3/(2\Delta_1\Delta_2)$  is the maximum Rabi coupling in Eq. (2). In Figure 4(a), we show the normalized three-photon coupling  $\Omega_{\rm eff}/\Omega_0$  over a wide range of detuning ratios  $\beta$ . We find excellent agreement with the expected coupling strength for the effective two-level system based on the inferred single-photon couplings (see Appendix A). For ratios close to  $\beta=1$ , direct excitation to  $^3P_1$  is no longer negligible and the observed Rabi frequencies are slightly lower than predicted. While the strong coupling near this divergence is desirable, sufficient detuning from the single-photon resonance is required to maintain efficient three-photon excitation. We achieve Rabi frequencies as high as  $50~\rm kHz$  while maintaining a detuning of over  $500~\rm natural$  linewidths.

We expect the three-photon coupling to depend on the shape of the effective orbital  $|{}^3\mathrm{P}_1,\theta_B\rangle$  and the projection of the light onto it [see Fig. 2(b)]. We define the maximum Rabi coupling at a given magnetic field  $\Omega_B \equiv \Omega_0 \, \sqrt{1+\beta^2}/(1-\beta^2)$ , such that the three-photon coupling becomes

$$\Omega_{\text{eff}} = \Omega_B \sin \theta_B, \quad \text{for } -\frac{\pi}{2} \le \theta_B \le \frac{\pi}{2}.$$
(7)

In Figure 4(b), we plot the previous dataset in the alternative parametrization  $\Omega_{\rm eff}/\Omega_B$  versus the projection angle  $\theta_B$ . This normalization avoids the divergence at  $\beta=1$  and shows the sinusoidal variation of the projection, which asymptotes to 1 for large values of  $\beta$ .

At a given  $\Omega_B$ , the coupling depends on the projection of the atom's dipole moment onto the light polarization vector. Tuning  $\theta_B$  has the same effect on the coupling as using a polarization for the second light field  $\mathbf{e}^{(2)}$  that is impossible to attain with collinear light. For a general elliptical polarization  $\mathbf{e}^{(2)} = \sin \theta \ \hat{\mathbf{x}} + i \cos \theta \ \hat{\mathbf{y}}$  with ellipticity an-



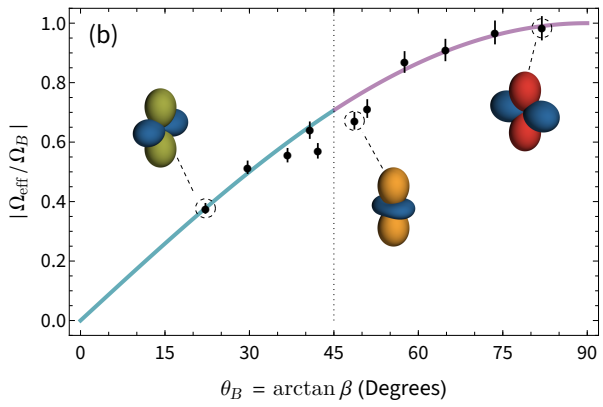


FIG. 4. Dimensionless three-photon coupling and projection angle. (a) Measured normalized Rabi frequencies  $|\Omega_{\rm eff}/\Omega_0|$  as a function of  $\beta$ , where  $\Omega_0$  is the predicted maximum coupling strength at  $\beta=0$ . Error bars indicate one standard deviation of the combined uncertainty in the measurement of  $\Omega_{\rm eff}$  and the theoretical prediction of  $\Omega_0$ . The solid curves correspond to the expected scaling from Eq. (6). The parameter space is divided into two distinct regions,  $\beta<1$  (teal) and  $\beta>1$  (purple). The coupling strength diverges at  $\beta=1$  (dotted line), which corresponds to the single-photon resonance to the  $|{}^3P_1,m=+1\rangle$  state. For this data, the laser detuning  $\Delta_1$  is always positive, but an identical divergence around the m=-1 state can be found for negative detunings. (b) The same data in a different normalization  $|\Omega_{\rm eff}/\Omega_B|$ , where  $\Omega_B$  is the maximum coupling at a given magnetic field, versus the projection angle  $\theta_B$ . This parametrization emphasizes the wave-plate-like rotation of the atom's effective dipole moment relative to the polarization of the light, as depicted in Fig. 2(b). The solid curve corresponds to the sinusoid in Eq. (7), with the same colored regions as in (a). Since there is no divergence in this parametrization, the slight deviation from the model around  $\theta_B=45^\circ$  (dotted line) is more apparent. The callouts show the shape of the effective wave function  $|{}^3P_1, \theta_B\rangle$  for a selection of data points.

gle  $\theta$  in the xy-plane, the three-photon coupling becomes  $\Omega_{\rm eff} = \Omega_B \cos(\theta_B - \theta)$ . In this work we use  $\theta = \pi/2$ , which is the only polarization choice compatible with collinear propagation along  $\hat{\mathbf{y}}$ . Thus, the external torque from the magnetic field tunes the effective dipole moment of the atom in much the same way as a wave plate rotates the polarization of light (see Appendix D 7).

Next, we demonstrate a proof-of-principle clock atom interferometer using the collinear three-photon transition [Fig. 5]. We apply a symmetric Mach-Zehnder pulse sequence [40] consisting of a beam splitter pulse  $(\pi/2)$ , followed by a mirror pulse  $(\pi)$ , and a recombination pulse  $(\pi/2)$ . These pulses are separated by an interrogation time  $T=200~\mu s$ . The visibility of the interferometer signal is maintained for interrogation times much longer than the intermediate state lifetimes, confirming coherent three-photon excitation of the long-lived clock state. This visibility can be improved by using a colder atomic ensemble as well as a larger beam size to reduce intensity inhomogeneity across the cloud.

This is the first demonstration of a  $^1\mathrm{S}_0 - ^3\mathrm{P}_0$  clock atom interferometer in  $^{88}\mathrm{Sr}$  without the use of a large magnetic bias field [36]. Compared to previous work, we observe a 30-fold increase in Rabi frequency using only 17% of the laser intensity and 3% of the magnetic field strength [41]. Because of the low magnetic field requirement, our method is applicable in long-baseline atom interferometers, where efficient atom-light interaction is desired anywhere along the baseline [42, 43]. Additionally, the small magnetic field amplitude sets a  $^3\mathrm{P}_0$  lifetime of over  $10^6$  s, significantly longer than the natural lifetime of 118 s in  $^{87}\mathrm{Sr}$  [44]. Long coherence times are essential for probing gravity [45] and detecting gravitational waves with long baselines [31, 38]. We also observe more

than ten times the Rabi frequency than what could be achieved on the naturally occurring <sup>87</sup>Sr clock transition with the same total intensity. High Rabi frequencies ensure broad velocity acceptance [46] and allow for more pulses in a given free-fall time, which is beneficial for any large momentum transfer (LMT) atom interferometer [43, 47], regardless of scale. LMT atom interferometry between the <sup>1</sup>S<sub>0</sub> and <sup>3</sup>P<sub>0</sub> clock states could now have utility in small-scale devices due to the speed advantage of three-photon atom optics, which relaxes the atom temperature requirements compared to Bragg transitions [48]. Moreover, a modified three-photon transition with the 679 nm beam counterpropagating with respect to the other two beams would yield a net momentum transfer of  $3 \, \hbar k$ per pulse, allowing for a larger sensitivity enhancement than two-photon atom optics for the same number of pulses. As such, LMT-enhanced three-photon clock atom interferometers can be employed in similar applications as compact Bragg and Raman atom interferometers, including gravimetry, gravity gradiometry, inertial navigation, and geodesy [49].

Next-generation long-baseline clock atom interferometer experiments, including MAGIS-100 [37] and AION [50], rely on LMT atom optics to significantly enhance their sensitivity. For these applications, interferometry pulses with transfer fidelities above 99% are required [46, 51]. Density matrix simulations suggest that our method can support such pulse efficiencies with W/cm²-scale laser intensities and magnetic fields below 10 G, yielding Rabi frequencies of at least 10 kHz (see Appendix B 2). This pulse fidelity could be reached by using a larger beam waist (e.g., in the millimeter range) to reduce intensity inhomogeneity across the cloud, combined with either a lower-temperature cloud, a velocity-selective initial pulse [43], or a composite pulse sequence to reduce

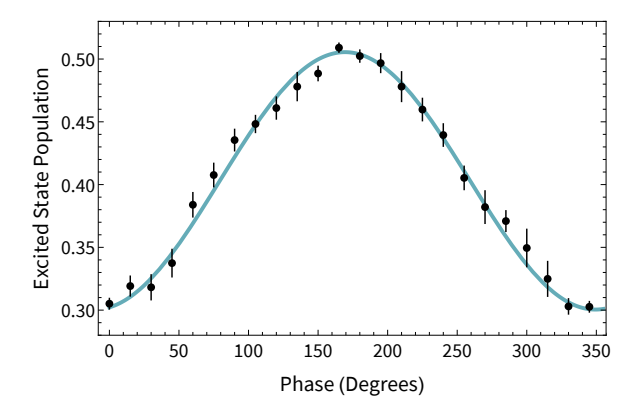


FIG. 5. A three-photon clock atom interferometer with bosonic  $^{88}$ Sr. Normalized  $^3P_0$  excited state population after a Mach-Zehnder pulse sequence versus the laser phase of the first pulse. The pulses are separated by an interrogation time  $T=200~\mu s$ . Every data point is the mean of ten measurements and error bars indicate the standard error of the mean. The solid line is a sinusoidal fit with a visibility (peak-to-peak amplitude) of 20.5(3)%. The three-photon pulses are applied with  $\Delta_1/2\pi=28.0(1)~\rm MHz$  and  $\delta\omega_B/2\pi=21.15(1)~\rm MHz$ .

Doppler broadening [52]. Moreover, collinear three-photon transitions enable the use of bosonic isotopes that feature higher natural abundance, simpler level structure, and reduced magnetic field sensitivity. All of these attributes are favorable for reaching the challenging sensitivity targets for gravitational wave detection and dark matter searches with clock atom interferometers.

Driving the  $^{1}S_{0}$ – $^{3}P_{0}$  clock transition in bosonic atoms also has many advantages in atomic clocks, including insensitivity to the polarization of trapping light, and lack of a first-order Zeeman shift [5, 17, 53]. Existing  $^{88}$ Sr clocks are limited by shifts from the second-order Zeeman effect and from the probe light [18,54–56]. The method described here employs a magnetic field strength that is substantially smaller per unit Rabi frequency, reducing the Zeeman shift for a given coupling strength. In addition, the overall probe light shift can be eliminated to first order with an appropriate choice of laser detunings (see Appendix A 5). Thus, the three-photon transition demonstrated here appears promising for improving the accuracy of bosonic clocks.

Many of these advantages are also favorable for applications in quantum information science [57], where the bosonic  $^3P_0$  [27, 29, 58, 59] and  $^3P_2$  [60, 61] states show promise for qubit storage and manipulation by leveraging their long coherence times and environmental insensitivity. While not demonstrated in this work, a similar three-photon excitation  $^1S_0 \rightarrow ^3P_1 \rightarrow ^3S_1 \rightarrow ^3P_2$  can be achieved by substituting 707 nm for 679 nm light [23], which may have advantages over magnetic quadrupole excitation to  $^3P_2$  [62,63].

The method demonstrated here is broadly applicable in other systems that use ultranarrow singlet-to-triplet transitions, especially when high Rabi coupling is beneficial and bosonic isotopes are preferred. In particular, precision measurements based on the differential interrogation of distant atoms benefit from the application of common, copropagating laser pulses.

*Note added.* – Upon completion of this manuscript, we became aware of related work on non-collinear three-photon transitions in Bose-Einstein condensates of <sup>84</sup>Sr [64].

## ACKNOWLEDGEMENTS

We wish to thank Mark Kasevich and Shaun Burd for helpful discussions. We thank Leo Hollberg for letting us use his frequency reference. B.G. acknowledges support from the Office of Naval Research through the NDSEG fellowship. This work was supported by the Gordon and Betty Moore Foundation Grant No. GBMF7945, the NSF QLCI Award No. OMA-2016244, and partially supported by the U.S. Department of Energy, Office of Science, National Quantum Information Science Research Centers, Superconducting Quantum Materials and Systems Center (SQMS) under Contract No. DE-AC02-07CH11359.

## APPENDIX A: METHODS

## 1. Experimental setup

We prepare a thermal ensemble of  $10^6$  <sup>88</sup>Sr atoms at a temperature of 2  $\mu$ K, using a two-stage magneto-optical trap (MOT). A more detailed description of the setup and experimental sequence for the atomic cloud preparation can be found in Ref. [47]. After the atoms are released from the final MOT, we turn off the magnetic quadrupole field and apply a constant bias field with an amplitude between 4 and 19 G. Then, a three-photon laser pulse of variable duration and detuning is applied to the atoms. The atomic cloud has an rms radius of 130(5)  $\mu$ m at the time of the pulse. The final atomic state is characterized using a state-selective imaging scheme described below.

The three-photon pulses consist of light from three external cavity diode lasers (ECDLs) at 689, 688, and 679 nm. Each ECDL is locked to an optical frequency comb (Menlo Systems FC1500-ULN) that is stabilized to an optical cavity (Menlo Systems 1550 ORS). From the sum of the residual error signals of these locks, we infer the rms frequency noise of  $\Delta_3/2\pi$  to be 11 kHz within the three-photon pulse bandwidth. The repetition rate of the comb is calibrated using Rabi spectroscopy on the  ${}^{1}S_{0} - {}^{3}P_{1}$  transition. The relative polarizations of the lasers are set by combining the beams on a polarizing beam splitter. The combined output is sent through an acousto-optic modulator and the diffracted order is coupled into a polarization-maintaining optical fiber. The final three-photon beam at the location of the atoms has a  $1/e^2$  radial waist of 392.5(3) µm. The average optical power in the desired linear polarizations are 0.79, 6.9, and 2.2 mW at 689, 688, and 679 nm, respectively.

The 679 nm laser detuning was held fixed for all experiments at -2536 MHz with respect to the  $^3P_0-^3S_1$  resonance, while the 689 nm detuning  $\Delta_1/2\pi$  was varied between 4 and 43 MHz. In each case, the 688 nm detuning was adjusted to achieve three-photon resonance ( $\Delta_{\text{eff}}=0$ ) for the given value

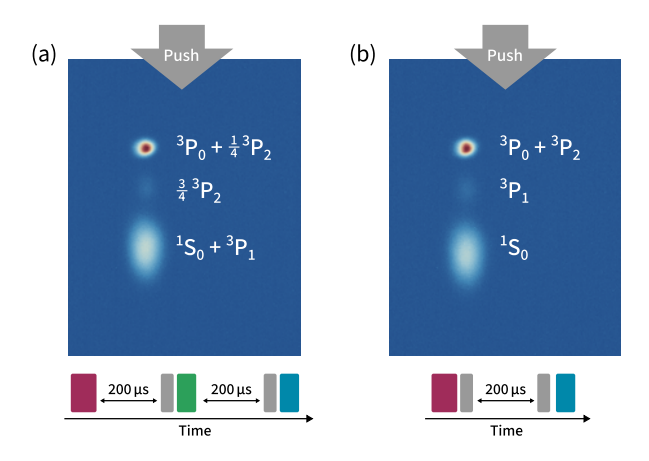


FIG. 6. State-selective imaging schemes. Each scheme produces three spatially separated clouds through the successive application of push pulses, as indicated in the pulse sequences below. Here, red indicates a three-photon pulse and gray a push pulse, while green (707 nm) and blue (679 + 707 nm) are repump pulses. (a) The first imaging scheme is designed to determine the  $^3P_0$  and  $^3P_2$  populations, while the  $^1S_0$  and  $^3P_1$  populations cannot be measured independently. (b) The second scheme measures the  $^3P_1$  and  $^1S_0$  populations.

of  $\Delta_1$ , with a range of  $-2556 \pm 22$  MHz with respect to the  $^3P_1 - ^3S_1$  resonance.

#### 2. State-selective imaging

To characterize the atomic state after a three-photon pulse, we spatially separate the atoms into three clouds using a sequence of push and repump pulses (see Fig. 6). Push pulses consist of 461 nm light resonant with the  ${}^{1}S_{0}-{}^{1}P_{1}$  transition, which imparts momentum to atoms in the ground state  ${}^{1}S_{0}$ . The first push pulse occurs 200 µs after the end of the threephoton pulse. This time is chosen to give atoms in the <sup>3</sup>P<sub>1</sub> state sufficient time to decay to the ground state. To optically pump atoms out of <sup>3</sup>P<sub>2</sub>, we apply a repump pulse resonant with the  ${}^{3}P_{2} - {}^{3}S_{1}$  transition at 707 nm. Because of the 3:1 branching ratio of this process, most of the atoms return to the ground state, while the rest are shelved in  ${}^{3}P_{0}$ . After an additional 200 µs, a second push pulse imparts momentum to the fraction of ground state atoms that were pumped out of <sup>3</sup>P<sub>2</sub> and adds additional momentum to the first pushed cloud. Finally, repump light at both 707 nm and 679 nm optically pumps all remaining atoms back into the ground state. We wait 4.5 ms for the three clouds to spatially separate and then count the number of atoms in each cloud using fluorescence imaging on the 461 nm transition. Because of the 3:1 branching ratio, the true  ${}^{3}P_{2}$  population is 4/3 of the raw atom number in the singly-pushed cloud. Conversely, the true  ${}^{3}P_{0}$  population is obtained by subtracting 1/3 of the atoms in the singly-pushed cloud from the nominal atom number in the unpushed cloud.

The  ${}^{3}P_{1}$  population is obtained using a modified version of the above imaging sequence (see Fig. 6(b)). A push pulse

immediately following the three-photon pulse separates unexcited ground state atoms from those anywhere in the  ${}^3P_J$  manifold. After a wait time of  $200~\mu s$ , a second push pulse imparts momentum to ground state atoms that have decayed from  ${}^3P_1$ . Finally, a repump pulse at both 707 and 679 nm optically pumps the combined populations of  ${}^3P_0$  and  ${}^3P_2$  back into the ground state. The atoms are then imaged after a 4.5~m s wait time as in the other scheme.

We count the populations using appropriate bins centered around each cloud pictured in Fig. 6. While the clouds are well separated, residual populations in neighboring bins can occur. Additionally, intensity inhomogeneity of the imaging beams causes a nonuniform scattering rate, leading to reduced counts, particularly for atoms in the  $^1\mathrm{S}_0$  bin. Small correction factors (approximately 10%) are applied to the totals to minimize the covariance between the total atom number and the Rabi oscillations.

## 3. Systematic errors

An important caveat to the  $^3P_1$  imaging sequence illustrated in Fig. 6(b) is that it undercounts the loss due to unwanted excitation, since atoms in this state can decay back into the ground state during the three-photon pulse. An estimate for the total loss due to off-resonant scattering from  $^3P_1$  is obtained from the number of scattering events N over the pulse duration  $t_p$ , given by

$$N = \frac{1}{\tau} \int_0^{t_p} P_e(t) dt \approx \frac{t_p}{\tau} \langle P_e \rangle.$$

Here,  $\tau$  is the lifetime and  $P_e(t)$  is the state population in  $^3P_1$ , with time-averaged fraction  $\langle P_e \rangle$ . For the data in Fig. 3(b), we estimate  $\langle P_e \rangle = 1.3(1)\%$  and N = 5.1(5)% for the total loss from this channel over the full 85  $\mu$ s.

We measure a laser polarization impurity of 2%, which can lead to parasitic excitation to the  $|{}^3P_1, m=0\rangle$  state if the 689 nm detuning is near resonance ( $\Delta_1=0$ ). We maintain a detuning of over 500 natural linewidths to avoid competing single-photon processes.

We observe transient magnetic field oscillations when turning on the bias magnetic field. We wait 4.5 ms for the field to settle before applying three-photon pulses. The magnetic field amplitudes B are obtained using Rabi spectroscopy of the  $^3P_1$  Zeeman splitting, which is given by  $\delta\omega_B=g_J\mu_BB/\hbar$ , where  $g_J=3/2$  is the Landé g factor and  $\mu_B$  is the Bohr magneton. We measure the Zeeman splittings at the start and  $100~\mu s$  after the three-photon pulse and observe a time variation of less than 1%.

### 4. Calculating the three-photon coupling

The expected three-photon Rabi frequencies are calculated using Eq. (3) and the three single-photon couplings

$$\Omega_i = \sqrt{\frac{6\pi c^2 \,\Gamma_{jk} \,I_i}{\hbar \,\omega_i^3}}, \quad \text{with } I_i = \frac{P_i}{\frac{\pi}{2} \,w_0^2}. \tag{A1}$$

TABLE I. Parameters for the relevant atomic transitions in  $^{88}$ Sr used to calculate the expected single-photon Rabi frequencies  $\Omega_i$ .

Transition $ j\rangle \leftrightarrow  k\rangle$	Wavelength	$\omega_i/2\pi$ (THz)	$\eta_{jk}$	$\tau_k$ (s)	$P_i$ (mW)	$\Omega_i/2\pi$ (MHz)
$ ^{1}S_{0}, m = 0\rangle \leftrightarrow  ^{3}P_{1}, m = \pm 1\rangle$	689 nm	434.829 121 311(010) [65]	1	$21.28(3) \times 10^{-6}$ [66]	0.79	1.239(1)
$ ^{3}P_{1}, m = \pm 1\rangle \leftrightarrow  ^{3}S_{1}, m = 0\rangle$	688 nm	435.731 697 200(500) [67]	1/6	$15.0(8) \times 10^{-9}$ [68]	6.9	56.0(4)
$ ^{3}P_{0}, m = 0\rangle \leftrightarrow  ^{3}S_{1}, m = 0\rangle$	$679~\mathrm{nm}$	441.332751300(700) [67]	1/9	13.0(6) × 10 [08]	2.2	35.8(3)

Here,  $I_i$  are the peak intensities of the Gaussian beams with  $1/e^2$  radial waist  $w_0$ , and  $P_i$  is the optical power in the spherical basis component that connects the specific m states [Fig. 1(b)]. The decay rate  $\Gamma_{jk}$  between states  $|k\rangle$  and  $|j\rangle$  is related to the lifetime of the excited state  $\tau_k$  by

$$\Gamma_{jk} = \eta_{jk} \frac{1}{\tau_k},\tag{A2}$$

where  $\eta_{jk}$  are the branching ratios, which can be calculated using Wigner 3-j and 6-j symbols [69]. Table I summarizes the parameters used to calculate the single-photon couplings, including the experimentally determined transition frequencies and lifetimes.

To calibrate the laser intensities, we drive resonant Rabi oscillations between  $\left|^{1}\mathrm{S}_{0}\right\rangle$  and  $\left|^{3}\mathrm{P}_{1},m=0\right\rangle$  with a measured optical power at 689 nm. The peak Rabi frequency from this measurement serves as an *in situ* measurement of the effective beam size, with a  $1/e^{2}$  radial waist of  $w_{0}=392.5(3)$  µm. This effective waist is then approximately common to all three wavelengths, since they are delivered via the same optical fiber and collimation optics.

The detuning of each laser from its respective atomic resonance is inferred using the frequency comb, which we calibrate with the observed 689 nm resonance frequency in conjunction with its best experimental estimate [65]. The uncertainties in  $\Delta_1$  and  $\Delta_2$  used to calculate  $\Omega_{\rm eff}$ ,  $\Omega_0$ , and  $\Omega_B$  reflect the combined uncertainties from our frequency comb measurements and the uncertainties in the literature transition frequencies [65,67]. Our uncertainty in the cumulative laser detuning  $\Delta_3$  is lower than the reported uncertainties for the 688 and 679 nm transition frequencies. We take advantage of the fact that their difference is equal to the energy splitting between the  $^3P_1$  and  $^3P_0$  states, which is known more precisely [65,70]. Our uncertainty in the effective three-photon detuning  $\Delta_{\rm eff}$ , which corresponds to the width of the shaded region in Fig. 3(a), reflects the combined uncertainties of  $\Delta_3$  and  $\Omega_{\rm ac}$ .

## 5. The ac-Stark shift

The three-photon transition experiences a net ac-Stark shift given by Eqs. (D20) and (D21). To lowest order, the shift is

$$\begin{split} \Omega_{\rm ac} &= -\Omega_0^{\rm ac} + \Omega_3^{\rm ac} \\ &= -\frac{|\Omega_1|^2}{2} \frac{\Delta_1}{\Delta_1^2 - \delta \omega_B^2} + \frac{|\Omega_3|^2}{4\Delta_2}. \end{split} \tag{A3}$$

The higher-order terms in Eqs. (D20) and (D21) are small compared to the lowest-order shifts and constitute a percent-level correction which we neglect here. In terms of the individual laser detunings  $\delta_1$  and  $\delta_2$  defined below [Eqs. (D2) to (D4)], Eq. (A3) is

$$\Omega_{\rm ac} = -\frac{|\Omega_1|^2}{2} \frac{\delta_1}{\delta_1^2 - \delta\omega_B^2} + \frac{|\Omega_3|^2}{4(\delta_1 + \delta_2)}.$$
 (A4)

Assuming fixed laser intensities, this shift vanishes for an appropriate choice of the 688 nm laser detuning, labeled  $\delta_2^*$ :

$$\delta_2^* = \delta_1 \left[ \frac{\Omega_3^2}{2\Omega_1^2} \left( 1 - \beta^2 \right) - 1 \right],$$
 (A5)

where, as usual,  $\beta=\delta\omega_B/\delta_1$ . Since the 679 nm transition is 3 orders of magnitude stronger than the 689 nm transition, the ratio  $\Omega_3^2/\Omega_1^2$  yields a large  $\delta_2^*$  for laser powers typically available in most experiments. Consequently, the ac-Stark shift-free condition can be fulfilled while maintaining a large detuning from  ${}^3\mathrm{S}_1$ .

## APPENDIX B: DENSITY MATRIX SIMULATIONS

# 1. Ensemble average

We simulate the three-photon dynamics by numerically solving the Lindblad master equation for all 13 magnetic sublevels of  $^{1}S_{0}$ ,  $^{3}S_{1}$ , and  $^{3}P_{J}$ , including all possible dipole-allowed transitions between the simulated states and excited state decay via spontaneous emission. We include the effects of intensity inhomogeneity and other broadening mechanisms by averaging the density matrix over variations in the single-photon Rabi frequencies and atom-laser detunings.

We denote r as the atom's radial position with respect to the peak intensity of the beam and  $\Delta$  as the detuning between the laser frequency and the atom's resonance frequency at rest. We take the normalized probability distributions in both coordinates to be Gaussian,

$$n(r) = \frac{1}{2\pi\sigma_r^2} e^{-r^2/2\sigma_r^2},$$
  
$$\mu(\Delta) = \frac{1}{\sqrt{2\pi}\sigma_\Delta} e^{-\Delta^2/2\sigma_\Delta^2},$$

where  $\sigma_r$  and  $\sigma_{\Delta}$  are the widths of the respective distributions. We label the density matrix of an atom at coordinates  $(r, \Delta)$ 

TABLE II. Damping rates of the three-photon Rabi oscillation in the averaged density matrix model [see Fig. 3(b)]. Damping mechanisms include off-resonant scattering (OS) from intermediate states in the three-photon process, as well as other technical contributions from laser frequency noise (LN), Doppler shifts (DS), and intensity inhomogeneity (IN).

Effects included	Damping rate (ms <sup>-1</sup> )	Curve in Fig. 7
OS (three-photon)	$1.2 \pm 0.1$	Purple
OS + LN	$4.3 \pm 0.5$	Orange
OS + LN + DS	$12.6 \pm 0.3$	Green
OS + LN + DS + IN	$36 \pm 2$	Blue

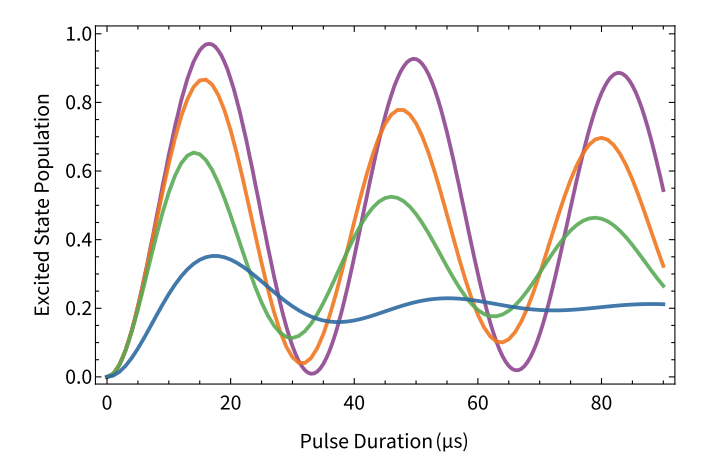


FIG. 7. Simulated Rabi oscillations in the presence of the damping mechanisms listed in Table II. The oscillation with all effects included (blue) corresponds to the mean density matrix prediction in Fig. 3(b). The peak transfer efficiencies are considerably higher without intensity inhomogeneity (green), and without intensity inhomogeneity or Doppler shifts (orange). The purple curve only includes damping from off-resonant scattering inherent in the three-photon process and features a peak transfer efficiency of 97%.

as  $\rho(t; r, \Delta)$ . The weighted average density matrix is then given by

$$\langle \rho(t) \rangle = \int_{-\infty}^{\infty} \int_{0}^{\infty} \rho(t; r, \Delta) \, n(r) \, \mu(\Delta) \, 2\pi r \, dr \, d\Delta.$$

We further assume that the lasers' intensity profiles are Gaussian, the single-photon Rabi frequencies vary in r according to

$$\Omega_i(r) = \Omega_i \ e^{-r^2/w_0^2},$$

where  $\Omega_i$  is the peak single-photon Rabi frequency, and  $w_0$  is the laser beam waist. For an atom with velocity v along the light propagation direction, the three lasers have detunings given by

$$\delta_i = \delta_{i,0} + k_i v + \delta \omega_i$$

where  $\delta_{i,0}$  is the nominal single-photon detuning for the  $i^{\text{th}}$  laser,  $k_i v$  is the Doppler shift for laser wave number  $k_i$ , and  $\delta \omega_i$  is a possible offset caused by laser frequency noise. For simplicity, we assume that the laser frequency is constant

but that  $\delta\omega_i$  can vary shot to shot. The primary effect of laser noise and the Doppler shift is to detune the three-photon resonance, resulting in  $\Delta_3=(\delta_{679,0}-\delta_{688,0}-\delta_{689,0})-\Delta$ , where  $\Delta\equiv(k_{689}+k_{688}-k_{679})v+(\delta\omega_{689}+\delta\omega_{688}-\delta\omega_{679})$  is the cumulative Doppler shift and laser noise. Furthermore, if we ignore independent effects of the different  $\delta_i$  (e.g., singlebeam ac-Stark shifts), then we can model the cumulative broadening of the three-photon transition by adding  $\Delta$  to any one of the three laser frequencies. In the simulation, we add the Doppler shift and noise to the 688 nm laser detuning, so that  $\delta_{688}=\delta_{688,0}+\Delta$  and we set  $\delta_i=\delta_{i,0}$  for the other lasers.

In Figure 7, we show the impact of each of the broadening effects included in the model used in Fig. 3(b). To quantify the contribution of each effect to the observed damping, in Table II we report the simulated damping rates for different combinations of broadening effects. In the absence of laser frequency noise, temperature-dependent Doppler shifts, and intensity inhomogeneities present in our experiment, the maximum state transfer fidelity of 97% is limited by the off-resonant scattering loss set by the laser parameters and magnetic field strength. The fidelity can therefore be improved substantially by appropriate choice of laser parameters in an optimized experiment.

## 2. Minimizing off-resonant scattering losses

In the ideal case where inhomogeneities are small, the transfer efficiency of a three-photon pulse is ultimately limited by off-resonant scattering from  $^3\mathrm{P}_1$  and  $^3\mathrm{S}_1$ . Since population in these states is primarily due to direct single-photon excitation, this loss is proportional to the 689 and 679 nm laser intensities. To first order, the 688 nm laser intensity does not contribute to scattering, and it only begins to contribute at second order via two-photon Raman scattering. This observation can be exploited to reduce off-resonant scattering loss at a given three-photon coupling strength by appropriate allocation of intensities (i.e., using higher intensity for 688 nm).

The instantaneous scattering rates for the two single-photon processes can be approximately modeled as

$$R(^{3}P_{1}) = \frac{1}{\tau_{1}}P_{1}(t)P_{0}(t),$$

$$R(^{3}S_{1}) = \frac{1}{\tau_{2}}P_{2}(t)P_{3}(t),$$
(B1)

where  $P_i(t)$  are the populations and  $\tau_k$  the lifetimes of states  $i=\{0,1,2,3\}=\{{}^1\mathrm{S}_0,{}^3\mathrm{P}_1,{}^3\mathrm{S}_1,{}^3\mathrm{P}_0\}$ . Here the initial and final states of the three-photon process,  $P_0(t)$  and  $P_3(t)$ , act as weighting factors that set the fraction of atoms that can participate in the single-photon processes driving  $P_1(t)$  and  $P_2(t)$  at any given time. When the scattering rate is small, the steady-state populations of  ${}^3\mathrm{P}_1$  and  ${}^3\mathrm{S}_1$  may be estimated from the two-level optical Bloch equations:

$$P_i = \frac{(\Omega_i/\Gamma_i)^2}{1 + 2(\Omega_i/\Gamma_i)^2 + (2\delta_i/\Gamma_i)^2} \approx \left(\frac{\Omega_i}{2\delta_i}\right)^2 \quad \text{for } i = 1, 2,$$
(B2)

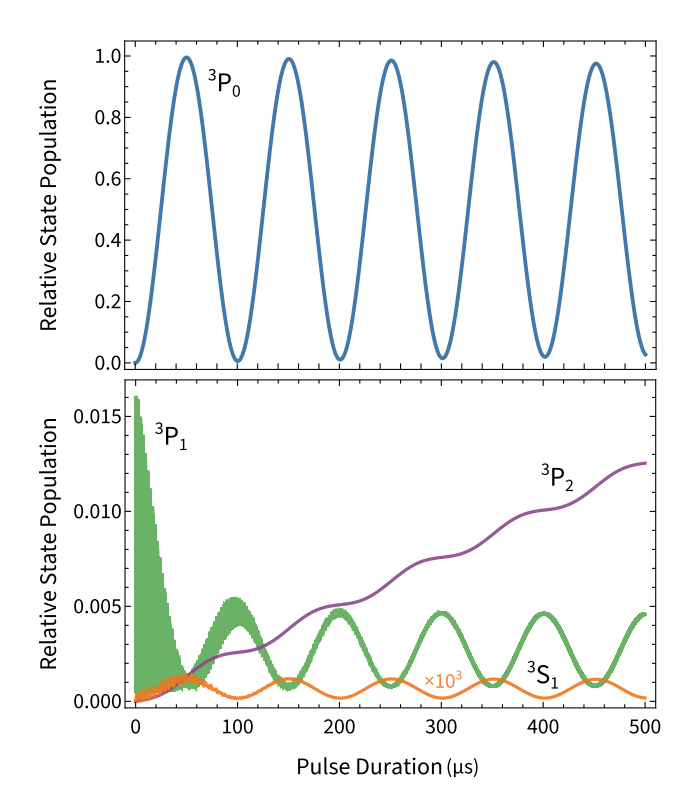


FIG. 8. Predicted populations in the relevant excited states from optimized density matrix simulations that minimize off-resonant scattering (parameters from third row in Table III). (a) A three-photon Rabi oscillation with a frequency of  $10~\rm kHz$  and peak transfer to the target state  $^3P_0$  (blue) of 99.5%. (b) Residual populations in  $^3P_1$  (green),  $^3P_2$  (purple), and  $^3S_1$  (orange). The small transient population in  $^3S_1$  is scaled up  $(\times 10^3)$  for visibility.

where in this limit the single-photon detunings  $\delta_i$  are much larger than  $\Omega_i$  and  $\Gamma_{jk}$ . Assuming a resonant three-photon excitation with minimal damping,

$$P_3(t) = \sin^2 \frac{\Omega_{\text{eff}} t}{2},$$
 (B3)  
 $P_0(t) = 1 - P_3(t).$ 

These can be inserted into Eq. (B1) and integrated up to  $t=t_\pi\equiv\pi/\Omega_{\rm eff}$  to give the estimated infidelity of a  $\pi$  pulse

$$N_{\rm scat} \approx \frac{\pi}{8\,\Omega_{\rm eff}} \left[ \frac{1}{\tau_2} \frac{\Omega_3^2}{\delta_3^2} + \frac{1}{\tau_1} \sum_{m=\pm 1} \frac{\Omega_1^2}{(\delta_1 + m\,\delta\omega_B)^2} \right]. \eqno(B4)$$

The assumption that the single-photon dynamics reach steady state within  $t_\pi$  is well justified for the  $^3P_0-^3S_1$  transition, since the lifetime of the upper state  $\tau_2\ll t_\pi$  and since  $\delta_3$  is several orders of magnitude larger than both  $\Omega_3$  and  $\Gamma_3$ . This steady-state approximation is less accurate for the narrow  $^1S_0-^3P_1$  transition. As a result, Eq. (B4) overestimates the loss due to scattering from  $^3P_1$ , but is nevertheless useful for calculating initial guesses for laser parameters which can be further optimized to yield high-fidelity Rabi oscillations in the density matrix simulation.

Table III details a few examples of parameters found for three-photon Rabi oscillations with reduced off-resonant scattering optimized using Eq. (B4). All examples maintain a high Rabi frequency ( $\Omega_{\rm eff}=2\pi\times 10~{\rm kHz}$ ) and use modest laser intensities (1 - 10 W/cm²) and magnetic field strengths (< 5 G). Figure 8 shows the result of a full density matrix simulation using one of these parameter sets, validating the loss model. These examples suggest that it is possible to achieve high-fidelity three-photon transitions between the  $^1{\rm S}_0$  and  $^3{\rm P}_0$  clock states while maintaining high Rabi frequency. By comparison, to reach the same coupling strength for the single-photon transition in  $^{87}{\rm Sr}$  would require about 10 times the total laser intensity assumed here.

Additionally, it is informative to compare the technical requirements for the three-photon approach to the magnetic-field-induced single-photon transition in bosons at 698 nm [15]. To achieve the same coupling strength at the same magnetic field level (5 G) would require a 698 nm laser intensity of more than  $10^7$  W/cm<sup>2</sup>. Alternatively, using the same total intensity assumed in Table III, reaching a Rabi frequency of 10 kHz would require magnetic field strengths from 5,000 to 11,000 G (0.5 to 1.1 T).

## APPENDIX C: FREQUENCY COMB CALIBRATION

## 1. Cumulative detuning $\Delta_3$

Using the definitions of the cumulative detunings Eqs. (D6) to (D8) with individual laser detunings  $\delta_1 = \delta_{689}$ ,  $\delta_2 = \delta_{688}$ , and  $\delta_3 = \delta_{679}$ , the total cumulative detuning  $\Delta_3$  is

$$\Delta_3 = \delta_{679} - (\delta_{689} + \delta_{688}) \tag{C1}$$

The uncertainties in the single-photon detunings are limited by the literature uncertainties in the respective transitions [65,67]. However, we can accurately calculate  $\Delta_3$  by taking advantage of the fact that the difference in the 679 and 688 nm transition frequencies is equal to the difference in the 689 and 698 nm transition frequencies, i.e.  $f_{679}-f_{688}=f_{689}-f_{698}$ . The latter two transitions are known to higher accuracy than the former two, which provides us with a significantly better estimate of the overall detuning. In terms of the frequency comb repetition rate  $f_{RR}$  and tooth integers  $n_i$ , the difference in these detunings is

$$\begin{split} \frac{\delta_{679} - \delta_{688}}{2\pi} &= (\delta f_{679} - \delta f_{688}) - (f_{689} - f_{698}) \\ &+ (n_{679} - n_{688}) f_{\rm RR} \end{split}$$

Here,  $\delta f_i$  is the beat note between the  $i^{\text{th}}$  laser and the nearest comb tooth  $n_i$ , and  $f_i$  is the (literature) resonance frequency of the  $i^{\text{th}}$  transition. We then have

$$\frac{\Delta_3}{2\pi} = (\delta f_{679} - \delta f_{688}) - \frac{\delta_{689}}{2\pi} - (f_{689} - f_{698}) + (n_{679} - n_{688}) f_{RR}$$
(C2)

This expression for  $\Delta_3$  is independent of the uncertainty in the 679 and 688 nm transition frequencies. Note that we have

TABLE III. Example parameters for three-photon Rabi oscillations with reduced off-resonant scattering. All parameter sets yield a Rabi frequency of  $\Omega_{\rm eff} = 2\pi \times 10$  kHz. By comparison, to achieve the same coupling strength in the single-photon  $^1{\rm S}_0 - ^3{\rm P}_0$  transition in  $^{87}{\rm Sr}$ , a peak intensity of approximately 70 W/cm² would be required. The magnitude of the laser detunings to the  $m=\pm 1$  magnetic sublevels of  $^3{\rm P}_1$  are given by  $|\Delta_1 \pm \delta \omega_B|$ , shown in the fifth column. For these simulations, we take  $\Delta_1=0$ .

$I_{689} \over (\mathrm{W/cm^2})$	$I_{688} \  m (W/cm^2)$	$I_{679} \  m (W/cm^2)$	$I_{ m Total} \ ({ m W/cm}^2)$	$\frac{ \Delta_1 \pm \delta\omega_B /2\pi}{(\text{MHz})}$	$\Delta_2/2\pi$ (GHz)	<i>B</i> (G)	Peak transfer (%)
0.13	1.75	0.09	1.97	6.3	-3.10	3.0	99.0
0.13	3.57	0.27	3.97	7.4	-6.50	3.5	99.2
0.13	8.98	0.45	9.55	8.4	-11.5	4.0	99.5

assumed here that the 679 and 688 nm lasers are are offset from resonance by the same number of comb teeth, as is the case in our experiment.

#### 2. Clock implementation

Here we briefly outline how the spectroscopic information obtained from observing the three-photon resonance could be combined with an optical frequency comb to realize a clock. In particular, we show conceptually how to stabilize a frequency comb to the atomic resonance. This process differs from a conventional optical atomic clock because there are now three different laser frequencies instead of one, and none of them are on resonance with the desired  $^1S_0 \rightarrow ^3P_0$  clock transition. Consider the cumulative three-photon detuning defined previously:

$$\begin{split} \Delta_{3} &= \delta_{3} - (\delta_{1} + \delta_{2}) \\ &= \left(\omega_{3} - (\omega_{|2,0\rangle}^{a} - \omega_{|3\rangle}^{a})\right) \\ &- \left(\omega_{1} - (\omega_{|1,0\rangle}^{a} - \omega_{|0\rangle}^{a}) + \omega_{2} - (\omega_{|2,0\rangle}^{a} - \omega_{|1,0\rangle}^{a})\right) \\ &= (\omega_{|3\rangle}^{a} - \omega_{|0\rangle}^{a}) - ((\omega_{1} + \omega_{2}) - \omega_{3}) \end{split}$$
(C3)

where we used the definitions of the detunings from Eqs. (D2) to (D4). In terms of the Sr transitions used in this work, the three laser frequencies are  $\omega_1 = \omega_{689}$ ,  $\omega_2 = \omega_{688}$ , and  $\omega_3 = \omega_{679}$ , and so we have

$$\Delta_3 = \omega_{698}^a - ((\omega_{689} + \omega_{688}) - \omega_{679}) \tag{C4}$$

where  $\omega_{698}^a \equiv \omega_{|3\rangle}^a - \omega_{|0\rangle}^a$  is the atomic energy splitting of the  $^1\mathrm{S}_0 \to {}^3\mathrm{P}_0$  clock transition at 698 nm. Thus,  $\Delta_3$  measures the difference between the energies of the three lasers and the desired clock transition that we wish to lock them to.

Performing spectroscopy on the three-photon transition results in a measurement of the effective three-photon detuning  $\Delta_{\rm eff}=\Delta_3-\Omega_0^{\rm ac}+\Omega_3^{\rm ac}$ . Assuming that the ac-Stark shift terms are appropriately stabilized, this measurement of  $\Delta_{\rm eff}$  then provides information that can be used to stabilize  $\Delta_3$  by applying feedback to any of the three lasers. As a concrete example, we could apply feedback to the 688 nm laser frequency  $\omega_{688}$  to lock  $\Delta_3=0$ . This would stabilize the linear combination of laser frequencies  $\omega_{689}+\omega_{688}-\omega_{679}$ , while leaving the other two linearly independent laser degrees of freedom unstabilized.

After stabilizing the lasers to the atom in this way, we would next stabilize the comb to the lasers in order to realize the clock. Consider the following beat note measurements between the three lasers and the nearest respective comb teeth:

$$\delta\omega_{689} = \omega_{689} - 2\pi (n_{689}f_{RR} + f_{ceo}) \tag{C5}$$

$$\delta\omega_{688} = \omega_{688} - 2\pi (n_{688} f_{RR} + f_{ceo}) \tag{C6}$$

$$\delta\omega_{679} = \omega_{679} - 2\pi(n_{679}f_{RR} + f_{ceo}) \tag{C7}$$

where  $n_{689}$ ,  $n_{688}$ , and  $n_{679}$  are the integer comb tooth indices,  $f_{\rm RR}$  is the comb repetition rate, and  $f_{\rm ceo}$  is the carrier-envelope offset frequency. By measuring each of these beat note frequencies, we construct the effective comb detuning  $\Delta_{\rm comb}$  defined as

$$\Delta_{\text{comb}} \equiv \delta\omega_{689} + \delta\omega_{688} - \delta\omega_{679} \tag{C8}$$

Note that  $\Delta_{comb}$  should be thought of as a measured quantity that derives from the three beat note measurements. Thus, the measured value of  $\Delta_{comb}$  can be used to provide feedback to stabilize the comb. Using the expressions above, we have

$$\Delta_{\text{comb}} = \omega_{689} + \omega_{688} - \omega_{679} - 2\pi \left( (n_{689} + n_{688} - n_{679}) f_{\text{RR}} + f_{\text{ceo}} \right)$$
 (C9)

Finally, using Eq. (C4) we have

$$\Delta_{\text{comb}} = \omega_{698}^a - 2\pi \Big( (n_{689} + n_{688} - n_{679}) f_{\text{RR}} + f_{\text{ceo}} \Big) - \Delta_3$$

Assuming  $\Delta_3=0$  because of the laser lock to the atom as described above, we see that  $\Delta_{\rm comb}$  depends only on the comb parameters  $f_{\rm RR}$  and  $f_{\rm ceo}$  and the known integers  $n_{689},\,n_{688},$  and  $n_{679}$ . Furthermore,  $(n_{689}+n_{688}-n_{679})f_{\rm RR}+f_{\rm ceo}$  is indeed the frequency of the nearest comb tooth to the 698 nm clock transition, and so  $\Delta_{\rm comb}$  measures the detuning of this comb tooth from the atomic energy  $\omega_{698}^a$ . Thus, the comb could be stabilized by applying feedback to  $f_{\rm RR}$  in order to lock  $\Delta_{\rm comb}=0$ .

# APPENDIX D: CALCULATION OF THE THREE-PHOTON COUPLING

## 1. Three-photon Rabi oscillations

Here we show that the dynamics of the three-photon transition reduces to an effective coupling between the two clock states  $^{1}\mathrm{S}_{0}$  and  $^{3}\mathrm{P}_{0}$ . We include all eight relevant atomic energy levels as well as the three laser fields. We then adiabatically eliminate the intermediate states, yielding an effective two-level system that undergoes Rabi oscillations.

The Hamiltonian for the multilevel atom is

$$\hat{H} = \hat{H}_a + \hat{V} \tag{D1}$$

where  $\hat{V} = -\hat{\boldsymbol{\mu}} \cdot \mathbf{E}(t)$  is the electric dipole coupling with electric dipole operator  $\hat{\boldsymbol{\mu}}$ , and  $\hat{H}_a$  is the atomic Hamiltonian that describes the internal degrees of freedom of the atom. The applied light electric field is

$$\mathbf{E}(t) = \sum_{\alpha=1}^{3} \mathrm{Re} \Big[ \widetilde{\mathbf{E}}_{\alpha} e^{i\omega_{\alpha} t} \Big] = \frac{1}{2} \sum_{\alpha=1}^{3} \Big( \widetilde{\mathbf{E}}_{\alpha} e^{i\omega_{\alpha} t} + \widetilde{\mathbf{E}}_{\alpha}^{*} e^{-i\omega_{\alpha} t} \Big)$$

where the  $\alpha$  sum is over the laser frequencies  $\omega_{\alpha}$  used to drive the three-photon transition. The components of the field amplitudes  $\widetilde{\mathbf{E}}_{\alpha}$  are, in general, complex to allow for arbitrary elliptical polarization. The atomic Hamiltonian has solutions of the form  $|\Phi_i(t)\rangle = |i\rangle \, e^{-i\omega_i^a t}$  which satisfy the Schrödinger equation  $i\hbar\partial_t \, |\Phi_i(t)\rangle = \hat{H}_a \, |\Phi_i(t)\rangle$ , where  $|i\rangle$  are the energy eigenstates of the atom with associated energy levels  $\hbar\omega_i^a$ .

Switching to the interaction picture, we write the state as  $|\psi(t)\rangle = \sum_i c_i(t) |\Phi_i(t)\rangle$  with time-dependent amplitudes  $c_i(t)$ . Substituting this into the full Schrödinger equation  $i\hbar \partial_t |\psi(t)\rangle = \hat{H} |\psi(t)\rangle$  then yields

$$\begin{split} \dot{c}_i &= \frac{1}{i\hbar} \sum_j c_j e^{i\omega_{ij}^a t} \left\langle i | \left( -\hat{\boldsymbol{\mu}} \cdot \mathbf{E}(t) \right) | j \right\rangle \\ \dot{c}_i &= \frac{1}{2i} \sum_{j,\alpha} c_j \left( \Omega_{ij}^{(\alpha)} e^{i(\omega_\alpha + \omega_{ij}^a)t} + \Omega_{ij}^{(\alpha*)} e^{-i(\omega_\alpha - \omega_{ij}^a)t} \right) \end{split}$$

where  $\Omega_{ij}^{(\alpha)} \equiv \frac{1}{\hbar} \left\langle i | \left( - \hat{\pmb{\mu}} \cdot \widetilde{\mathbf{E}}_{\alpha} \right) | j \right\rangle$  is the Rabi coupling between levels  $|i \rangle$  and  $|j \rangle$  of field  $\widetilde{\mathbf{E}}_{\alpha}$  and  $\omega_{ij}^a \equiv \omega_i^a - \omega_j^a$  is their energy difference. Similarly,  $\Omega_{ij}^{(\alpha*)} \equiv \frac{1}{\hbar} \left\langle i | \left( - \hat{\pmb{\mu}} \cdot \widetilde{\mathbf{E}}_{\alpha}^* \right) | j \right\rangle$  and we have  $\left( \Omega_{ij}^{(\alpha)} \right)^* = \Omega_{ji}^{(\alpha*)}$ .

To model the three-photon dynamics, we consider the following states of the Sr atom:  $|0\rangle \equiv |^1 S_0\rangle$ ,  $|1, m_1\rangle \equiv |^3 P_1, m_1\rangle$ ,  $|2, m_2\rangle \equiv |^3 S_1, m_2\rangle$ ,  $|3\rangle \equiv |^3 P_0\rangle$ . Here,  $m_1$  and  $m_2$  label the magnetic sublevels for states  $|1\rangle$  and  $|2\rangle$ , respectively, and both range from -1 to +1. This results in a set of eight coupled equations,

$$\begin{split} \dot{c}_0 &= \frac{1}{2i} \sum_{j,\alpha} \, c_j \Big( \Omega_{0j}^{(\alpha)} \, e^{i(\omega_\alpha + \omega_{0j}^a)t} + \Omega_{0j}^{(\alpha*)} \, e^{-i(\omega_\alpha - \omega_{0j}^a)t} \Big) \\ \dot{c}_{1,m_1} &= \frac{1}{2i} \sum_{j,\alpha} \, c_j \Big( \Omega_{1m_1j}^{(\alpha)} \, e^{i(\omega_\alpha + \omega_{1m_1j}^a)t} \\ &\qquad \qquad + \Omega_{1m_1j}^{(\alpha*)} \, e^{-i(\omega_\alpha - \omega_{1m_1j}^a)t} \Big) \\ \dot{c}_{2,m_2} &= \frac{1}{2i} \sum_{j,\alpha} \, c_j \Big( \Omega_{2m_2j}^{(\alpha)} \, e^{i(\omega_\alpha + \omega_{2m_2j}^a)t} \\ &\qquad \qquad + \Omega_{2m_2j}^{(\alpha*)} \, e^{-i(\omega_\alpha - \omega_{2m_2j}^a)t} \Big) \\ \dot{c}_3 &= \frac{1}{2i} \sum_{j,\alpha} \, c_j \Big( \Omega_{3j}^{(\alpha)} \, e^{i(\omega_\alpha + \omega_{3j}^a)t} + \Omega_{3j}^{(\alpha*)} \, e^{-i(\omega_\alpha - \omega_{3j}^a)t} \Big) \end{split}$$

where we adopt the following subscript convention for the couplings and energy differences involving the  $|1,m_1\rangle$  and  $|2,m_2\rangle$  states:  $\Omega_{1m_1j}^{(\alpha)}=\frac{1}{\hbar}\left\langle 1,m_1\right|\left(-\hat{\boldsymbol{\mu}}\cdot\widetilde{\mathbf{E}}_{\alpha}\right)|j\rangle,\,\Omega_{2m_2j}^{(\alpha)}=\frac{1}{\hbar}\left\langle 2,m_2\right|\left(-\hat{\boldsymbol{\mu}}\cdot\widetilde{\mathbf{E}}_{\alpha}\right)|j\rangle,\,\omega_{1m_1j}^a=\omega_{|1,m_1\rangle}^a-\omega_j,$  and  $\omega_{2m_2j}^a=\omega_{|2,m_2\rangle}^a-\omega_j.$  To simplify, we take advantage of the fact that each laser frequency interacts strongly only with a limited number of states. We consider only the following coupling terms:

$$\begin{split} \Omega_{0m_{1}}^{(1)} &= \frac{1}{\hbar} \left\langle 0 | \left( -\boldsymbol{\mu} \cdot \widetilde{\mathbf{E}}_{1} \right) | 1, m_{1} \right\rangle \\ \Omega_{1m_{1}2m_{2}}^{(2)} &= \frac{1}{\hbar} \left\langle 1, m_{1} | \left( -\boldsymbol{\mu} \cdot \widetilde{\mathbf{E}}_{2} \right) | 2, m_{2} \right\rangle \\ \Omega_{3m_{2}}^{(3)} &= \frac{1}{\hbar} \left\langle 3 | \left( -\boldsymbol{\mu} \cdot \widetilde{\mathbf{E}}_{3} \right) | 2, m_{2} \right\rangle \end{split}$$

and we take all other  $\Omega_{ij}^{\alpha}$  to be zero. With this restriction, we simplify subscripts  $1m_1 \to m_1$  and  $2m_2 \to m_2$  whenever there is no ambiguity. After making the rotating wave approximation we find

$$\begin{split} \dot{c}_0 &= \frac{1}{2i} \sum_{m_1} \Omega_{0m_1}^{(1)} c_{1,m_1} e^{i(\omega_1 - \omega_{m_10}^a)t} \\ \dot{c}_{1,m_1} &= \frac{1}{2i} \Omega_{m_10}^{(1*)} c_0 e^{-i(\omega_1 - \omega_{m_10}^a)t} \\ &+ \frac{1}{2i} \sum_{m_2} \Omega_{1m_12m_2}^{(2)} c_{2,m_2} e^{i(\omega_2 - \omega_{2m_21m_1}^a)t} \\ \dot{c}_{2,m_2} &= \frac{1}{2i} \Omega_{m_23}^{(3*)} c_3 e^{-i(\omega_3 - \omega_{m_23}^a)t} \\ &+ \frac{1}{2i} \sum_{m_1} \Omega_{2m_21m_1}^{(2*)} c_{1,m_1} e^{-i(\omega_2 - \omega_{2m_21m_1}^a)t} \\ \dot{c}_3 &= \frac{1}{2i} \sum_{m_2} \Omega_{3m_2}^{(3)} c_{2,m_2} e^{i(\omega_3 - \omega_{m_23}^a)t} \end{split}$$

where  $\omega_{2m_21m_1}^a=\omega_{|2,m_2\rangle}^a-\omega_{|1,m_1\rangle}^a>0$ . We now define the detuning of each laser from the respective  $m_1=0$  and  $m_2=0$  states:

$$\delta_1 \equiv \omega_1 - (\omega_{|1,0\rangle}^a - \omega_{|0\rangle}^a) = \omega_1 - \omega_{|0\rangle}^a \tag{D2}$$

$$\delta_2 \equiv \omega_2 - (\omega_{|2,0\rangle}^a - \omega_{|1,0\rangle}^a) = \omega_2 - \omega_{2010}^a$$
 (D3)

$$\delta_3 \equiv \omega_3 - (\omega^a_{|2,0\rangle} - \omega^a_{|3\rangle}) = \omega_3 - \omega^a_{03}$$
 (D4)

In the experiment, the detuning  $\delta_2$  must always be much greater than the Zeeman splittings of the  $|1,m_1\rangle$  and  $|2,m_2\rangle$  levels to avoid off-resonant scattering losses from  $|2,m_2\rangle$ . As a result, we can neglect these Zeeman splittings to a good approximation and assume  $(\omega_2 - \omega_{2m_21m_1}^a) \approx \delta_2$ . Likewise,  $\delta_3$  is also much larger than the Zeeman splitting of  $|2,m_2\rangle$  so we have  $(\omega_3 - \omega_{m_23}^a) \approx \delta_3$ . In contrast, the Zeeman shift of  $|1,m_1\rangle$  is comparable to  $\delta_1$  and cannot be neglected:

$$\Delta_{1,m_1} \equiv \omega_1 - \omega_{m_10}^a = \delta_1 - m_1 \delta \omega_B \tag{D5}$$

where  $\delta\omega_B$  is the Zeeman splitting between  $|1,1\rangle$  and  $|1,0\rangle$ ,

$$\dot{c}_0 = \frac{1}{2i} \sum_{m_1} \Omega_{0m_1}^{(1)} c_{1,m_1} e^{i\Delta_{1,m_1} t}$$

$$\dot{c}_{1,m_1} = \frac{1}{2i} \Omega_{m_10}^{(1*)} c_0 e^{-i\Delta_{1,m_1} t} + \frac{1}{2i} e^{i\delta_2 t} \sum_{m_2} \Omega_{1m_1 2m_2}^{(2)} c_{2,m_2}$$

$$\dot{c}_{2,m_2} = \frac{1}{2i} \Omega_{m_23}^{(3*)} c_3 e^{-i\delta_3 t} + \frac{1}{2i} e^{-i\delta_2 t} \sum_{m_1} \Omega_{2m_2 1m_1}^{(2*)} c_{1,m_1}$$

$$\dot{c}_3 = \frac{1}{2i} \sum_{m_2} \Omega_{3m_2}^{(3)} c_{2,m_2} e^{i\delta_3 t}$$

For convenience, we introduce the cumulative detunings from each of the three m=0 states,

$$\Delta_1 \equiv \delta_1 \tag{D6}$$

$$\Delta_2 \equiv \delta_1 + \delta_2 \tag{D7}$$

$$\Delta_3 \equiv \delta_3 - (\delta_1 + \delta_2) \tag{D8}$$

Next, we eliminate the explicit time dependence by performing the following unitary transformation:

$$\widetilde{c}_{0}(t) = c_{0}(t)$$

$$\widetilde{c}_{1,m_{1}}(t) = c_{1,m_{1}}(t)e^{i\Delta_{1,m_{1}}t}$$

$$\widetilde{c}_{2,m_{2}}(t) = c_{2,m_{2}}(t)e^{i\Delta_{2}t}$$

$$\widetilde{c}_{3}(t) = c_{3}(t)e^{-i\Delta_{3}t}$$
(D9)

which results in

$$\dot{\tilde{c}}_{0} = \frac{1}{2i} \sum_{m_{1}} \Omega_{0m_{1}}^{(1)} \tilde{c}_{1,m_{1}}$$

$$\dot{\tilde{c}}_{1,m_{1}} = i\Delta_{1,m_{1}} \tilde{c}_{1,m_{1}} + \frac{1}{2i} \Omega_{m_{1}0}^{(1*)} \tilde{c}_{0} + \frac{1}{2i} \sum_{m_{2}} \Omega_{1m_{1}2m_{2}}^{(2)} \tilde{c}_{2,m_{2}}$$

$$\dot{\tilde{c}}_{2,m_{2}} = i\Delta_{2} \tilde{c}_{2,m_{2}} + \frac{1}{2i} \Omega_{m_{2}3}^{(3*)} \tilde{c}_{3} + \frac{1}{2i} \sum_{m_{1}} \Omega_{2m_{2}1m_{1}}^{(2*)} \tilde{c}_{1,m_{1}}$$

$$\dot{\tilde{c}}_{3} = -i\Delta_{3} \tilde{c}_{3} + \frac{1}{2i} \sum_{m_{2}} \Omega_{3m_{2}}^{(3)} \tilde{c}_{2,m_{2}}$$

Assuming that direct transitions to the intermediate states are sufficiently far detuned, we can now adiabatically eliminate the intermediate states since  $|\dot{\widetilde{c}}_{1,m_1}| \ll |\Delta_{1,m_1}\widetilde{c}_{1,m_1}|$  and  $|\dot{\widetilde{c}}_{2,m_2}| \ll |\Delta_2\,\widetilde{c}_{2,m_2}|$ . Taking  $\dot{\widetilde{c}}_{1,m_1} \approx 0$  and  $\dot{\widetilde{c}}_{2,m_2} \approx 0$  and solving gives

$$\widetilde{c}_{1,m_1} \approx \frac{\Omega_{m_10}^{(1*)}}{2\Delta_{1,m_1}} \widetilde{c}_0 + \frac{1}{2\Delta_{1,m_1}} \sum_{m_2} \Omega_{1m_12m_2}^{(2)} \widetilde{c}_{2,m_2} \quad (D10)$$

$$\widetilde{c}_{2,m_2} \approx \frac{\Omega_{m_2}^{(3*)}}{2\Delta_2} \widetilde{c}_3 + \frac{1}{2\Delta_2} \sum_{m_1} \Omega_{2m_21m_1}^{(2*)} \widetilde{c}_{1,m_1}$$
 (D11)

These equations are still coupled. To solve for  $\tilde{c}_{1,m_1}$  and  $\tilde{c}_{2,m_1}$  explicitly, we first substitute each equation into the other to

get a set of independent equations for  $|1, m_1\rangle$  and  $|2, m_2\rangle$ :

$$\widetilde{c}_{1,m_{1}} \approx \frac{\Omega_{m_{1}0}^{(1*)}}{2\Delta_{1,m_{1}}} \widetilde{c}_{0} + \sum_{m_{2}} \frac{\Omega_{1m_{1}2m_{2}}^{(2)} \Omega_{m_{2}3}^{(3*)}}{4\Delta_{1,m_{1}}\Delta_{2}} \widetilde{c}_{3} 
+ \sum_{m_{1}'} \sum_{m_{2}} \frac{\Omega_{1m_{1}2m_{2}}^{(2)} \Omega_{2m_{2}1m_{1}'}^{(2*)}}{4\Delta_{1,m_{1}}\Delta_{2}} \widetilde{c}_{1,m_{1}'} 
\widetilde{c}_{2,m_{2}} \approx \frac{\Omega_{m_{2}3}^{(3*)}}{2\Delta_{2}} \widetilde{c}_{3} + \sum_{m_{1}} \frac{\Omega_{2m_{2}1m_{1}}^{(2*)} \Omega_{m_{1}0}^{(1*)}}{4\Delta_{1,m_{1}}\Delta_{2}} \widetilde{c}_{0} 
+ \sum_{m_{2}'} \sum_{m_{1}} \frac{\Omega_{2m_{2}1m_{1}}^{(2*)} \Omega_{1m_{1}2m_{2}'}^{(2)}}{4\Delta_{1,m_{1}}\Delta_{2}} \widetilde{c}_{2,m_{2}'}$$
(D12)

A direct solution for  $\tilde{c}_{1,m_1}$  and  $\tilde{c}_{2,m_2}$  from these equations would be unwieldy, and we require only an approximate solution. To make a controlled approximation, it is helpful to substitute in Eqs. (D10) to (D11) one more time, yielding

$$\begin{split} \widetilde{c}_{1,m_{1}} \approx & \frac{\Omega_{m_{1}0}^{(1*)}}{2\Delta_{1,m_{1}}} \widetilde{c}_{0} + \sum_{m_{2}} \frac{\Omega_{1m_{1}2m_{2}}^{(2)}\Omega_{m_{2}3}^{(3*)}}{4\Delta_{1,m_{1}}\Delta_{2}} \widetilde{c}_{3} \\ & + \sum_{m_{1}^{\prime},m_{2}} \frac{\Omega_{1m_{1}2m_{2}}^{(2)}\Omega_{2m_{2}1m_{1}^{\prime}}^{(2*)}\Omega_{m_{1}^{\prime}0}^{(1*)}}{8\Delta_{1,m_{1}}\Delta_{1,m_{1}^{\prime}}\Delta_{2}} \widetilde{c}_{0} \\ & + \sum_{m_{1}^{\prime},m_{2}^{\prime}} \frac{\Omega_{1m_{1}2m_{2}}^{(2)}\Omega_{2m_{2}1m_{1}^{\prime}}^{(2*)}\Omega_{1m_{1}^{\prime}2m_{2}^{\prime}}^{(2)}}{8\Delta_{1,m_{1}}\Delta_{1,m_{1}^{\prime}}\Delta_{2}} \widetilde{c}_{2,m_{2}^{\prime}} \\ \widetilde{c}_{2,m_{2}} \approx & \frac{\Omega_{m_{2}3}^{(3*)}}{2\Delta_{2}}\widetilde{c}_{3} + \sum_{m_{1}} \frac{\Omega_{2m_{2}1m_{1}}^{(2*)}\Omega_{m_{1}0}^{(1*)}}{4\Delta_{1,m_{1}}\Delta_{2}} \widetilde{c}_{0} \\ & + \sum_{m_{2}^{\prime},m_{1}} \frac{\Omega_{2m_{2}1m_{1}}^{(2*)}\Omega_{1m_{1}2m_{2}^{\prime}}^{(3*)}\Omega_{m_{2}^{\prime}3}^{(3*)}}{8\Delta_{1,m_{1}}\Delta_{2}^{2}} \widetilde{c}_{3} \\ & + \sum_{m_{2}^{\prime},m_{1}^{\prime}} \frac{\Omega_{2m_{2}1m_{1}}^{(2*)}\Omega_{1m_{1}2m_{2}^{\prime}}^{(2)}\Omega_{2m_{2}^{\prime}1m_{1}^{\prime}}^{(2*)}}{8\Delta_{1,m_{1}}\Delta_{2}^{2}} \widetilde{c}_{1,m_{1}^{\prime}} \widetilde{c}_{1,m_{1}^{\prime}} \end{aligned}$$

We could continue to repeat this substitution process to generate additional terms. However, we see that this is indeed a decaying series, since  $\frac{\Omega}{\delta} \ll 1$  for any coupling  $\Omega$  and detuning  $\delta$ , and this small ratio appears with a higher power in each additional term. As a result, we may safely drop the last term in the above expressions.

$$\widetilde{c}_{1,m_{1}} \approx \frac{\Omega_{m_{1}0}^{(1*)}}{2\Delta_{1,m_{1}}} \widetilde{c}_{0} + \sum_{m_{2}} \frac{\Omega_{1m_{1}2m_{2}}^{(2)} \Omega_{m_{2}3}^{(3*)}}{4\Delta_{1,m_{1}}\Delta_{2}} \widetilde{c}_{3}$$

$$+ \sum_{m'_{1},m_{2}} \frac{\Omega_{1m_{1}2m_{2}}^{(2)} \Omega_{2m_{2}1m'_{1}}^{(2*)} \Omega_{m'_{1}0}^{(1*)}}{8\Delta_{1,m_{1}}\Delta_{1,m'_{1}}\Delta_{2}} \widetilde{c}_{0} \qquad (D13)$$

$$\widetilde{c}_{2,m_{2}} \approx \frac{\Omega_{m_{2}3}^{(3*)}}{2\Delta_{2}} \widetilde{c}_{3} + \sum_{m_{1}} \frac{\Omega_{2m_{2}1m_{1}}^{(2*)} \Omega_{m_{1}0}^{(1*)}}{4\Delta_{1,m_{1}}\Delta_{2}} \widetilde{c}_{0}$$

$$+ \sum_{m'_{2},m_{1}} \frac{\Omega_{2m_{2}1m_{1}}^{(2*)} \Omega_{1m_{1}2m'_{2}}^{(2)} \Omega_{m'_{2}3}^{(3*)}}{8\Delta_{1,m_{1}}\Delta_{2}^{2}} \widetilde{c}_{3} \qquad (D14)$$

We are ultimately interested in studying the effective two-level dynamics between levels  $|0\rangle$  and  $|3\rangle$  once the intermediate states have been adiabatically eliminated:

$$\dot{\tilde{c}}_0 = \frac{1}{2i} \sum_{m_1} \Omega_{0m_1}^{(1)} \tilde{c}_{1,m_1}$$
 (D15)

$$\dot{\tilde{c}}_3 = -i\Delta_3 \, \tilde{c}_3 + \frac{1}{2i} \sum_{m_2} \Omega^{(3)}_{3m_2} \tilde{c}_{2,m_2} \tag{D16}$$

Substituting the approximate solutions for  $\widetilde{c}_{1,m_1}$  and  $\widetilde{c}_{2,m_2}$ ,

$$\begin{split} \dot{\widetilde{c}}_{0} &= -i \sum_{m_{1}} \frac{\Omega_{0m_{1}}^{(1)} \Omega_{m_{1}0}^{(1*)}}{4\Delta_{1,m_{1}}} \widetilde{c}_{0} \\ &+ \frac{1}{2i} \sum_{m_{1},m_{2}} \frac{\Omega_{0m_{1}}^{(1)} \Omega_{1m_{1}2m_{2}}^{(2)} \Omega_{m_{2}3}^{(3*)}}{4\Delta_{1,m_{1}}\Delta_{2}} \widetilde{c}_{3} \\ &- i \sum_{m_{1},m_{1}',m_{2}} \frac{\Omega_{0m_{1}}^{(1)} \Omega_{1m_{1}2m_{2}}^{(2)} \Omega_{2m_{2}1m_{1}'}^{(2*)} \Omega_{m_{1}'0}^{(1*)}}{16\Delta_{1,m_{1}}\Delta_{1,m_{1}'}\Delta_{2}} \widetilde{c}_{0} \quad \text{(D17)} \\ \dot{\widetilde{c}}_{3} &= -i\Delta_{3} \, \widetilde{c}_{3} - i \sum_{m_{2}} \frac{\Omega_{3m_{2}}^{(3)} \Omega_{m_{2}3}^{(3*)}}{4\Delta_{2}} \widetilde{c}_{3} \\ &+ \frac{1}{2i} \sum_{m_{1},m_{2}} \frac{\Omega_{3m_{2}}^{(3)} \Omega_{2m_{2}1m_{1}}^{(2*)} \Omega_{m_{1}0}^{(1*)}}{4\Delta_{1,m_{1}}\Delta_{2}} \widetilde{c}_{0} \\ &- i \sum_{m_{2},m_{2}',m_{1}} \frac{\Omega_{3m_{2}}^{(3)} \Omega_{2m_{2}1m_{1}}^{(2*)} \Omega_{1m_{1}2m_{2}'}^{(3)} \Omega_{m_{2}'3}^{(3*)}}{16\Delta_{1,m_{1}}\Delta_{2}^{2}} \widetilde{c}_{3} \quad \text{(D18)} \end{split}$$

We now define the following:

$$\Omega_{\text{eff}} \equiv \sum_{m_1, m_2} \frac{\Omega_{3m_2}^{(3)} \Omega_{2m_2 1 m_1}^{(2*)} \Omega_{m_1 0}^{(1*)}}{4\Delta_{1, m_1} \Delta_2}$$
(D19)

$$\Omega_0^{\rm ac} \equiv \sum_{m_1} \frac{|\Omega_{0m_1}^{(1)}|^2}{4\Delta_{1,m_1}} + \sum_{m_1,m_1',m_2} \frac{\Omega_{0m_1}^{(1)}\Omega_{1m_12m_2}^{(2)}\Omega_{2m_21m_1'}^{(2*)}\Omega_{m_1'0}^{(1*)}}{16\Delta_{1,m_1}\Delta_{1,m_1'}\Delta_2} \tag{D20}$$

$$\Omega_{3}^{\text{ac}} \equiv \sum_{m_{2}} \frac{|\Omega_{3m_{2}}^{(3)}|^{2}}{4\Delta_{2}} + \sum_{m_{2},m_{2}',m_{1}} \frac{\Omega_{3m_{2}}^{(3)} \Omega_{2m_{2}1m_{1}}^{(2*)} \Omega_{1m_{1}2m_{2}'}^{(2)} \Omega_{m_{2}'3}^{(3*)}}{16\Delta_{1,m_{1}} \Delta_{2}^{2}}$$
(D21)

where  $\Omega_{\text{eff}}$  is the effective three-photon Rabi frequency, and  $\Omega_0^{\text{ac}}$  and  $\Omega_3^{\text{ac}}$  are ac-Stark shifts of the states  $|0\rangle$  and  $|3\rangle$ , respectively. The effective two-level dynamics have the form

$$\dot{\tilde{c}}_0 = -i\,\Omega_0^{\rm ac}\,\tilde{c}_0 + \frac{\Omega_{\rm eff}^*}{2i}\tilde{c}_3 \tag{D22}$$

$$\dot{\widetilde{c}}_3 = -i\left(\Delta_3 + \Omega_3^{\rm ac}\right)\widetilde{c}_3 + \frac{\Omega_{\rm eff}}{2i}\widetilde{c}_0 \tag{D23}$$

It is helpful to perform another unitary transformation

$$\widetilde{c}_0 = \overline{c}_0 e^{-\frac{i}{2}(\Delta_3 + \Omega_3^{\text{ac}} + \Omega_0^{\text{ac}})t} \tag{D24}$$

$$\widetilde{c}_3 = \overline{c}_3 e^{-\frac{i}{2}(\Delta_3 + \Omega_3^{\text{ac}} + \Omega_0^{\text{ac}})t} \tag{D25}$$

which results in a symmetric set of equations

$$\partial_t \begin{pmatrix} \overline{c}_0 \\ \overline{c}_3 \end{pmatrix} = \frac{1}{2i} \begin{pmatrix} -\Delta_{\text{eff}} & \Omega_{\text{eff}}^* \\ \Omega_{\text{eff}} & \Delta_{\text{eff}} \end{pmatrix} \begin{pmatrix} \overline{c}_0 \\ \overline{c}_3 \end{pmatrix}$$
(D26)

where  $\Delta_{\rm eff} \equiv \Delta_3 + \Omega_{\rm ac}$  is the three-photon detuning and  $\Omega_{\rm ac} \equiv -\Omega_0^{\rm ac} + \Omega_3^{\rm ac}$  is the net ac-Stark shift. This system behaves as an effective two-level atom that will Rabi oscillate between states  $|0\rangle$  and  $|3\rangle$  with resonant Rabi frequency  $\Omega_{\rm eff}$  and detuning  $\Delta_{\rm eff}$ .

In terms of the dipole matrix elements, the effective threephoton Rabi coupling has the form

$$\Omega_{\text{eff}} = \sum_{m_1, m_2} \frac{\langle 3 | \boldsymbol{\mu} \cdot \widetilde{\mathbf{E}}_3 | 2, m_2 \rangle \langle 2, m_2 | \boldsymbol{\mu} \cdot \widetilde{\mathbf{E}}_2^* | 1, m_1 \rangle \langle 1, m_1 | \boldsymbol{\mu} \cdot \widetilde{\mathbf{E}}_1^* | 0 \rangle}{4\Delta_{1, m_1} \Delta_2 \hbar^3}$$
(D27)

or equivalently, in terms of the Sr energy levels

$$\Omega_{\text{eff}} = \sum_{m_1, m_2} \frac{\langle^3 P_0 | \hat{\boldsymbol{\mu}} \cdot \widetilde{\mathbf{E}}_3 |^3 S_1, m_2 \rangle \langle^3 S_1, m_2 | \hat{\boldsymbol{\mu}} \cdot \widetilde{\mathbf{E}}_2^* |^3 P_1, m_1 \rangle \langle^3 P_1, m_1 | \hat{\boldsymbol{\mu}} \cdot \widetilde{\mathbf{E}}_1^* |^1 S_0 \rangle}{4\Delta_{1, m_1} \Delta_2 \hbar^3}$$
(D28)

## 2. Cartesian basis for J=1

When computing the three-photon coupling for linearly polarized light, it is convenient to express the angular momentum states using the Cartesian basis. On the other hand, the energy level shifts from the magnetic field are most naturally described in the usual spherical basis. To help evaluate the dipole matrix elements for the intermediate states in Eq. (D28), we consider states with angular momentum J=1 and their representation in both the spherical and Cartesian bases. Here,  $\bf J$  is a placeholder for any angular momentum, so the following applies to spin  $\bf S$  and orbital  $\bf L$ , as well as for total angular momentum  $\bf J=\bf L+\bf S$ .

In the spherical basis for J=1, the three states that form a complete basis are denoted as  $|+1\rangle \equiv |J=1,m=1\rangle_z$ ,

 $|-1\rangle\equiv |J=1,m=-1\rangle_z$ , and  $|0\rangle\equiv |J=1,m=0\rangle_z$ , where the subscript indicates that these spherical states are projections along the  $\hat{\mathbf{z}}$  axis. Although less common, it is also possible to use spherical basis states with respect to the  $\hat{\mathbf{x}}$  or  $\hat{\mathbf{y}}$  axes. We define a set of Cartesian basis states that are linear combinations of the  $\hat{\mathbf{z}}$  projection states:

$$|J_x\rangle \equiv |J=1, m=0\rangle_x = \frac{-|+1\rangle + |-1\rangle}{\sqrt{2}}$$
 (D29)

$$|J_y\rangle \equiv |J=1, m=0\rangle_y = \frac{|+1\rangle + |-1\rangle}{-i\sqrt{2}} \tag{D30}$$

$$|J_z\rangle \equiv |J=1, m=0\rangle_z = |0\rangle$$
 (D31)

As indicated, the  $|J_x\rangle$  and  $|J_y\rangle$  basis states correspond to zero projection of angular momentum along the  $\hat{\mathbf{x}}$  and  $\hat{\mathbf{y}}$  axes, analogous to  $|J=1,m=0\rangle_z$  in the spherical basis. These  $|J_n\rangle$  Cartesian states are symmetric with respect to the  $\hat{\mathbf{x}}$ ,  $\hat{\mathbf{y}}$ ,  $\hat{\mathbf{z}}$  axes and form a complete basis for the J=1 states that is complementary to the spherical basis:  $\sum_{n=1}^{3} |J_n\rangle \langle J_n| = \sum_{m=-1}^{+1} |m\rangle \langle m| = 1$ . The Cartesian states arise naturally when an atom is driven by linearly polarized light, since in this

case an atom initially in an L=0 state  $|0,0\rangle_\ell$  will transition to a  $|J_n\rangle$  state, as we will see below. To transform between these two bases, we compute the amplitudes  $\langle m|J_n\rangle$ , which may be represented in matrix form as

$$U_{mn} \equiv \langle m|J_n\rangle \doteq \begin{pmatrix} \frac{-1}{\sqrt{2}} & \frac{i}{\sqrt{2}} & 0\\ \frac{1}{\sqrt{2}} & \frac{i}{\sqrt{2}} & 0\\ 0 & 0 & 1 \end{pmatrix}$$
(D32)

where we use the following conventions for the state representations:  $\langle +1| \doteq (1,0,0), \langle -1| \doteq (0,1,0), \langle 0| \doteq (0,0,1),$  for the  $|m\rangle$  states and  $|J_x\rangle \doteq (1,0,0)^\intercal$ ,  $|J_y\rangle \doteq (0,1,0)^\intercal$ ,  $|J_z\rangle \doteq (0,0,1)^\intercal$  for the Cartesian states. Note that the unconventional ordering of the  $|0\rangle$  and  $|-1\rangle$  states in this matrix representation is chosen so that the  $|J_z\rangle$  and  $|0\rangle$  states agree. Also, as expected, the basis transformation  $U_{mn}$  is unitary with  $U^\dagger U = 1$ .

We can now express the three-photon coupling  $\Omega_{\rm eff}$  in the Cartesian basis. To begin, the detuning denominator  $\Delta_{1,m_1}$  in Eq. (D28) can be written as a diagonal matrix in the spherical basis:

$$\Omega_{\mathrm{eff}} = \sum_{m_1, m_1', m_2} \frac{\left<^3 \mathbf{P}_0 \right| \left(\hat{\boldsymbol{\mu}} \cdot \widetilde{\mathbf{E}}_3\right) \left|^3 \mathbf{S}_1, m_2 \right> \left<^3 \mathbf{S}_1, m_2 \right| \left(\hat{\boldsymbol{\mu}} \cdot \widetilde{\mathbf{E}}_2^*\right) \left|^3 \mathbf{P}_1, m_1' \right> \left< m_1' \right| \hat{\boldsymbol{T}} \left| m_1 \right> \left<^3 \mathbf{P}_1, m_1 \right| \left(\hat{\boldsymbol{\mu}} \cdot \widetilde{\mathbf{E}}_1^*\right) \left|^1 \mathbf{S}_0 \right> \left|^3 \mathbf{P}_1, m_1' \right> \left< m_1' \right> \left|^3 \mathbf{P}_1, m_1' \right> \left< m_1' \right> \left|^3 \mathbf{P}_1, m_1' \right> \left|^3 \mathbf{P$$

where we define the matrix  $\langle m_1'|\hat{T}|m_1\rangle$  as the inverse of the detunings of the  $^3\mathrm{P}_1$  state. Explicitly we have  $T_{m_1',m_1}\equiv\langle m_1'|\hat{T}|m_1\rangle$  and

$$T_{m_1',m_1} \doteq \begin{pmatrix} \frac{1}{\Delta_{1,1}} & 0 & 0\\ 0 & \frac{1}{\Delta_{1,-1}} & 0\\ 0 & 0 & \frac{1}{\Delta_{1,0}} \end{pmatrix} = \begin{pmatrix} \frac{1}{\Delta_1 - \delta\omega_B} & 0 & 0\\ 0 & \frac{1}{\Delta_1 + \delta\omega_B} & 0\\ 0 & 0 & \frac{1}{\Delta_1} \end{pmatrix}$$

where, as before,  $\Delta_1$  is the detuning of  $\mathbf{E}_1$  from  $|^3\mathrm{P}_1, m_1 = 0\rangle$  while  $\pm \delta \omega_B = \pm g_J \mu_B B/\hbar$  is the Zeeman detuning of the  $m_1 = \pm 1$  states, which is linearly proportional to the applied magnetic field. For  $^3\mathrm{P}_1$ , the Landé g factor  $g_J = 3/2$ .

Since the  $|J_n\rangle$  form a complete basis, the sum over  $m_2$  in  $\Omega_{\rm eff}$  may be written as  $\sum_{m_2}|^3{\rm S}_1,m_2\rangle\,\langle^3{\rm S}_1,m_2|=\sum_{l=1}^3|^3{\rm S}_1,J_l\rangle\,\langle^3{\rm S}_1,J_l|$ . Similarly, we can express the  $m_1$  and  $m_1'$  sums in the Cartesian basis by inserting the identity

$$\sum_{m_{1},m'_{1}} |{}^{3}P_{1}, m'_{1}\rangle T_{m'_{1},m_{1}} \langle {}^{3}P_{1}, m_{1}| = \sum_{m_{1},m'_{1}} \left( \sum_{j=1}^{3} |J_{j}\rangle \langle J_{j}| \right) |{}^{3}P_{1}, m'_{1}\rangle T_{m'_{1},m_{1}} \langle {}^{3}P_{1}, m_{1}| \left( \sum_{n=1}^{3} |J_{n}\rangle \langle J_{n}| \right)$$

$$= \sum_{j,n} |{}^{3}P_{1}, J_{j}\rangle D_{jn} \langle {}^{3}P_{1}, J_{n}|$$
(D34)

where  $D_{jn} \equiv \sum_{m_1,m_1'} \langle J_j | m_1' \rangle T_{m_1',m_1} \langle m_1 | J_n \rangle = \sum_{m_1,m_1'} (U_{m_1',j})^{\dagger} T_{m_1',m_1} U_{m_1,n}$ . Explicitly, we find

$$D_{jn} \doteq \begin{pmatrix} \frac{\Delta_1}{\Delta_1^2 - \delta\omega_B^2} & \frac{-i\delta\omega_B}{\Delta_1^2 - \delta\omega_B^2} & 0\\ \frac{i\delta\omega_B}{\Delta_1^2 - \delta\omega_B^2} & \frac{\Delta_1}{\Delta_1^2 - \delta\omega_B^2} & 0\\ 0 & 0 & \frac{1}{\Delta_1} \end{pmatrix}$$
(D35)

This matrix encodes the magnetic-field-induced mixing of the Cartesian orbital described in the main text. In particular, the off-diagonal entries of this matrix are responsible for allowing the three-photon transition to proceed using collinear light, as further described below. With these substitutions, the three-photon coupling becomes

$$\Omega_{\text{eff}} = \sum_{l,j,n} \frac{\langle {}^{3}P_{0}|\,\hat{\boldsymbol{\mu}} \cdot \widetilde{\mathbf{E}}_{3}\,|{}^{3}S_{1}, J_{l}\rangle\,\langle {}^{3}S_{1}, J_{l}|\,\hat{\boldsymbol{\mu}} \cdot \widetilde{\mathbf{E}}_{2}^{*}\,|{}^{3}P_{1}, J_{j}\rangle\,D_{jn}\,\langle {}^{3}P_{1}, J_{n}|\,\hat{\boldsymbol{\mu}} \cdot \widetilde{\mathbf{E}}_{1}^{*}\,|{}^{1}S_{0}\rangle}{4\Delta_{2}\hbar^{3}}$$
(D36)

#### 3. Decomposition of the states into L and S

Next we consider each of the four energy levels that enter into the three-photon coupling and express the states in terms of  $\bf L$  and  $\bf S$  angular momentum components.

 $^{1}S_{0}$ 

The ground state  $|^1S_0\rangle$  has L=0 and S=0, which we write as

$$|^{1}S_{0}\rangle = ||^{1}S_{0}|\rangle |0,0\rangle_{\ell} |0,0\rangle_{s}$$
 (D37)

where  $||^1 S_0|\rangle$  denotes the radial part of the  $|^1 S_0|$  state, i.e. the nonangular part. Here  $|j,m\rangle_J$  is a spherical basis state with angular momentum j and z projection m, and the J subscript indicates either orbital  $J=\ell$  or spin J=s. This notation will be used for the other states as well.

 $^3P_1$ 

Because of the LS coupling, the  $|^3\mathrm{P}_1\rangle$  state is not an eigenstate of S, but consists of a mixture of two bare states (before LS mixing), each with J=1. In terms of the bare states:

$$|^{3}P_{1}\rangle = a |^{3}P_{1}^{(0)}\rangle + b |^{1}P_{1}^{(0)}\rangle$$
 (D38)

where a and b are the amplitudes of the  $|^3\mathrm{P}_1^{(0)}\rangle$  (triplet) and  $|^1\mathrm{P}_1^{(0)}\rangle$  (singlet) bare-state contributions, respectively. First,  $|^1\mathrm{P}_1^{(0)}\rangle$  has L=1 and S=0, so in the Cartesian basis we have

$$|{}^{1}P_{1}^{(0)}, J_{n}\rangle = ||{}^{1}P_{1}^{(0)}|\rangle |L_{n}\rangle |0, 0\rangle_{s}$$
 (D39)

Now consider the triplet component  $|{}^{3}P_{1}^{(0)}, m\rangle$ . In the spherical basis, we can use Clebsch-Gordan coefficients to express the angular momentum state in terms of L=1 and S=1 states and their projections along  $\hat{\mathbf{z}}$ :

$$\begin{split} |J=1,m=1\rangle_z &= \frac{|1,1\rangle_\ell\,|1,0\rangle_s - |1,0\rangle_\ell\,|1,1\rangle_s}{\sqrt{2}} \quad \text{(D40)} \\ |J=1,m=-1\rangle_z &= \frac{-\,|1,-1\rangle_\ell\,|1,0\rangle_s + |1,0\rangle_\ell\,|1,-1\rangle_s}{\sqrt{2}} \end{split}$$

$$|J=1,m=0\rangle_z=\frac{|1,1\rangle_\ell\,|1,-1\rangle_s-|1,-1\rangle_\ell\,|1,1\rangle_s}{\sqrt{2}} \tag{D42}$$

Using Eqs. (D29) to (D31), we can convert these states to the Cartesian basis, using  $|1,\pm 1\rangle_\ell = \frac{1}{\sqrt{2}}(\mp |L_x\rangle - i |L_y\rangle)$ ,  $|1,0\rangle_\ell = |L_z\rangle$  and  $|1,\pm 1\rangle_s = \frac{1}{\sqrt{2}}(\mp |S_x\rangle - i |S_y\rangle)$ ,  $|1,0\rangle_s = |S_z\rangle$ . Thus the J=1 state for the triplet component can be written as

$$|J_n\rangle = \frac{i}{\sqrt{2}} \epsilon_{npq} |L_p\rangle |S_q\rangle$$
 (D43)

where  $\epsilon_{npq}$  is the Levi-Civita symbol and the sums over p and q are implied. Overall this yields

$$|^{3}P_{1}, J_{n}\rangle = a \left| |^{3}P_{1}^{(0)}| \right\rangle \frac{i}{\sqrt{2}} \epsilon_{npq} \left| L_{p} \right\rangle \left| S_{q} \right\rangle$$
$$+ b \left| |^{1}P_{1}^{(0)}| \right\rangle \left| L_{n} \right\rangle \left| 0, 0 \right\rangle_{s} \tag{D44}$$

 $^3\mathrm{S}_1$ 

The  $|^3S_1\rangle$  state has L=0 and S=1. We can decompose the state in terms of the **L** and **S** states in the spherical  $\hat{\mathbf{z}}$  basis as

$$|^{3}S_{1}, m\rangle = ||^{3}S_{1}|\rangle |0, 0\rangle_{\ell} |1, m\rangle_{s}$$
 (D45)

In terms of the Cartesian basis the state is then

$$|{}^{3}S_{1}, J_{n}\rangle = ||{}^{3}S_{1}|\rangle |0, 0\rangle_{\ell} |S_{n}\rangle$$
 (D46)

 $^{3}P_{0}$ 

The  $|^{3}P_{0}\rangle$  state has L=1, S=1, and J=0. In the spherical basis we have

$$\begin{split} |J=0,m=0\rangle &= \frac{1}{\sqrt{3}} \Big( |1,1\rangle_{\ell} \, |1,-1\rangle_{s} - |1,0\rangle_{\ell} \, |1,0\rangle_{s} \\ &+ |1,-1\rangle_{\ell} \, |1,1\rangle_{s} \Big) \end{split} \tag{D47}$$

which in the Cartesian basis is

$$|J=0, m=0\rangle = \frac{-1}{\sqrt{3}} \sum_{n} |L_n\rangle |S_n\rangle$$
 (D48)

The complete state in the Cartesian basis is then

$$|^{3}P_{0}, J = 0, m = 0\rangle = ||^{3}P_{0}|\rangle |J = 0, m = 0\rangle$$
  
=  $\frac{-1}{\sqrt{3}} ||^{3}P_{0}|\rangle \sum_{n} |L_{n}\rangle |S_{n}\rangle$  (D49)

## 4. Dipole matrix elements

Since the dipole operator  $\hat{\mu}$  does not operate on S states, only components of the two states with the same S state can contribute to the dipole matrix element. In evaluating the matrix elements below, we will take advantage of the fact that the  $|S_i\rangle$  states with S=1 are an orthonormal set and are also

orthogonal to the S=0 state:

$$\langle S_i | S_j \rangle = \delta_{ij} \tag{D50}$$

$$_{s}\langle 0,0|S_{i}\rangle = 0$$
 (D51)

The matrix element for the  $E_1$  coupling is

$$\langle^{3}\mathbf{P}_{1}, J_{n} | \hat{\boldsymbol{\mu}} \cdot \widetilde{\mathbf{E}}_{1}^{*} |^{1}\mathbf{S}_{0} \rangle = \left( a^{*} \langle |^{3}\mathbf{P}_{1}^{(0)}| | \frac{-i}{\sqrt{2}} \epsilon_{npq} \langle L_{p} | \langle S_{q} | + b^{*} \langle |^{1}\mathbf{P}_{1}^{(0)}| | \langle L_{n} | \langle 0, 0 |_{s} \rangle \hat{\boldsymbol{\mu}} \cdot \widetilde{\mathbf{E}}_{1}^{*} | |^{1}\mathbf{S}_{0} | \rangle |0, 0\rangle_{\ell} |0, 0\rangle_{s}$$

$$= b^{*} \langle |^{1}\mathbf{P}_{1}^{(0)}| | \langle L_{n} | \hat{\boldsymbol{\mu}} \cdot \widetilde{\mathbf{E}}_{1}^{*} | |^{1}\mathbf{S}_{0} | \rangle |0, 0\rangle_{\ell}$$
(D52)

The matrix element for  $\mathbf{E}_2$  is

$$\langle^{3}\mathbf{S}_{1}, J_{l} | \hat{\boldsymbol{\mu}} \cdot \widetilde{\mathbf{E}}_{2}^{*} |^{3}\mathbf{P}_{1}, J_{j} \rangle = \langle |^{3}\mathbf{S}_{1} ||_{\ell} \langle 0, 0 | \langle S_{l} | \hat{\boldsymbol{\mu}} \cdot \widetilde{\mathbf{E}}_{2}^{*} \left( a ||^{3}\mathbf{P}_{1}^{(0)}| \rangle \frac{i}{\sqrt{2}} \epsilon_{jkq} |L_{k} \rangle |S_{q} \rangle + b ||^{1}\mathbf{P}_{1}^{(0)}| \rangle |L_{j} \rangle |0, 0 \rangle_{s}$$

$$= \frac{ia}{\sqrt{2}} \epsilon_{jkq} \langle |^{3}\mathbf{S}_{1}||_{\ell} \langle 0, 0 | \hat{\boldsymbol{\mu}} \cdot \widetilde{\mathbf{E}}_{2}^{*} ||^{3}\mathbf{P}_{1}^{(0)}| \rangle |L_{k} \rangle \langle S_{l} |S_{q} \rangle$$

$$= \frac{ia}{\sqrt{2}} \epsilon_{jkl} \langle |^{3}\mathbf{S}_{1}||_{\ell} \langle 0, 0 | \hat{\boldsymbol{\mu}} \cdot \widetilde{\mathbf{E}}_{2}^{*} ||^{3}\mathbf{P}_{1}^{(0)}| \rangle |L_{k} \rangle$$
(D53)

where we first used  $\langle S_l | S_q \rangle = \delta_{lq}$  and then performed the sum over q. Similarly, the matrix element for  $\mathbf{E}_3$  is

$$\langle^{3}\mathbf{P}_{0}|\,\hat{\boldsymbol{\mu}}\cdot\widetilde{\mathbf{E}}_{3}\,|^{3}\mathbf{S}_{1},J_{l}\rangle = \left(\frac{-1}{\sqrt{3}}\,\langle|^{3}\mathbf{P}_{0}||\sum_{n}\langle L_{n}|\,\langle S_{n}|\right)\hat{\boldsymbol{\mu}}\cdot\widetilde{\mathbf{E}}_{3}\,||^{3}\mathbf{S}_{1}|\rangle\,|0,0\rangle_{\ell}\,|S_{l}\rangle$$

$$= \frac{-1}{\sqrt{3}}\,\langle|^{3}\mathbf{P}_{0}||\,\langle L_{l}|\,\hat{\boldsymbol{\mu}}\cdot\widetilde{\mathbf{E}}_{3}\,||^{3}\mathbf{S}_{1}|\rangle\,|0,0\rangle_{\ell}$$
(D54)

Collecting these results:

$$\langle {}^{3}\mathrm{P}_{1}, J_{n} | \, \hat{\boldsymbol{\mu}} \cdot \widetilde{\mathbf{E}}_{1}^{*} \, | {}^{1}\mathrm{S}_{0} \rangle = b^{*} \, \langle |{}^{1}\mathrm{P}_{1}^{(0)}| | \, \langle L_{n} | \, \hat{\boldsymbol{\mu}} \cdot \widetilde{\mathbf{E}}_{1}^{*} \, | |{}^{1}\mathrm{S}_{0}| \rangle \, |0, 0\rangle_{\ell} \tag{D55}$$

$$\langle {}^{3}\mathbf{S}_{1}, J_{l} | \hat{\boldsymbol{\mu}} \cdot \widetilde{\mathbf{E}}_{2}^{*} | {}^{3}\mathbf{P}_{1}, J_{j} \rangle = \frac{ia}{\sqrt{2}} \epsilon_{jkl} \langle |{}^{3}\mathbf{S}_{1}| | {}_{\ell} \langle 0, 0 | \hat{\boldsymbol{\mu}} \cdot \widetilde{\mathbf{E}}_{2}^{*} | |{}^{3}\mathbf{P}_{1}^{(0)} | \rangle | L_{k} \rangle$$
(D56)

$$\langle^{3}\mathbf{P}_{0}|\,\hat{\boldsymbol{\mu}}\cdot\widetilde{\mathbf{E}}_{3}\,|^{3}\mathbf{S}_{1},J_{i}\rangle = \frac{-1}{\sqrt{3}}\langle|^{3}\mathbf{P}_{0}||\,\langle L_{i}|\,\hat{\boldsymbol{\mu}}\cdot\widetilde{\mathbf{E}}_{3}\,||^{3}\mathbf{S}_{1}|\rangle\,|0,0\rangle_{\ell} \tag{D57}$$

Next, we define polarization unit vectors  $\mathbf{e}^{(\alpha)}$ , where  $\alpha=1,2,3$  corresponds to the three laser fields such that  $\widetilde{\mathbf{E}}_{\alpha}\equiv E^{(\alpha)}\mathbf{e}^{(\alpha)}$ , where  $E^{(\alpha)}$  is the field magnitude. The polarization unit vectors are normalized so that  $(\mathbf{e}^{(\alpha)})^*\cdot\mathbf{e}^{(\alpha)}=1$ . The dipole matrix operator for laser field  $\alpha$  is then  $\hat{\mu}\cdot\widetilde{\mathbf{E}}_{\alpha}=E^{(\alpha)}\sum_n\hat{\mu}_ne_n^{(\alpha)}$ , where the sum over n is over the Cartesian components  $e_n^{(\alpha)}$  of the polarization vector of laser  $\alpha$ , and  $\hat{\mu}_n$  are the Cartesian components of the dipole operator. Note that while the components  $e_n^{(\alpha)}$  may be complex for general elliptically polarized light, they are real for linear polarized light.

The Cartesian components of the dipole operator couple the L=0 state to L=1 states in the Cartesian basis:

$$\langle L_k | \hat{\mu}_n | 0, 0 \rangle_{\ell} = \hat{\mu} \, \delta_{kn} \tag{D58}$$

where  $\hat{\mu} \equiv |\hat{\mu}|$  is the magnitude of the dipole operator, which encodes the radial degree of freedom of the atom's internal state. When evaluating each of the matrix elements we therefore have

$$\langle L_k | \hat{\boldsymbol{\mu}} \cdot \widetilde{\mathbf{E}}_{\alpha} | 0, 0 \rangle_{\ell} = E^{(\alpha)} \sum_{n} \langle L_k | \hat{\mu}_n e_n^{(\alpha)} | 0, 0 \rangle_{\ell}$$
$$= E^{(\alpha)} \sum_{n} \hat{\mu} \, \delta_{kn} e_n^{(\alpha)} = E^{(\alpha)} \hat{\mu} \, e_k^{(\alpha)}$$

which implies that a linearly polarized light field couples the L=0 state to the L=1 Cartesian state that is aligned with the polarization direction. With this, the complete dipole

matrix elements are

$$\langle {}^{3}\mathbf{P}_{1}, J_{n} | \hat{\boldsymbol{\mu}} \cdot \widetilde{\mathbf{E}}_{1}^{*} | {}^{1}\mathbf{S}_{0} \rangle = b^{*}E^{(1)} \langle | {}^{1}\mathbf{P}_{1}^{(0)} | | \hat{\mu} | | {}^{1}\mathbf{S}_{0} | \rangle (e_{n}^{(1)})^{*}$$

$$\langle {}^{3}\mathbf{S}_{1}, J_{l} | \hat{\boldsymbol{\mu}} \cdot \widetilde{\mathbf{E}}_{2}^{*} | {}^{3}\mathbf{P}_{1}, J_{j} \rangle = \frac{iaE^{(2)}}{\sqrt{2}} \sum_{k} \epsilon_{jkl} \langle | {}^{3}\mathbf{S}_{1} | | \hat{\mu} | | {}^{3}\mathbf{P}_{1}^{(0)} | \rangle (e_{k}^{(2)})^{*}$$

$$\langle {}^{3}\mathbf{P}_{0} | \hat{\boldsymbol{\mu}} \cdot \widetilde{\mathbf{E}}_{3} | {}^{3}\mathbf{S}_{1}, J_{l} \rangle = \frac{-E^{(3)}}{\sqrt{3}} \langle | {}^{3}\mathbf{P}_{0} | | \hat{\mu} | | {}^{3}\mathbf{S}_{1} | \rangle e_{l}^{(3)}$$
(D59)

Up to this point, we allow for general  $\tilde{\mathbf{E}}_{\alpha}$  with arbitrary polarization  $\mathbf{e}^{(\alpha)}$ . However, in our definition of the single-photon Rabi couplings  $\Omega_i$  between the intermediate levels, it is convenient to choose a normalization convention that is consistent with the specific polarizations chosen experimentally. In particular, in the main text we focus on the polarization sequence  $\hat{\mathbf{x}} - \hat{\mathbf{x}} - \hat{\mathbf{z}}$  for the three photons. In this case we have  $\tilde{\mathbf{E}}_1 = E^{(1)}\hat{\mathbf{x}} = \mathbf{E}_1^{(+)} + \mathbf{E}_1^{(-)}$  and  $\tilde{\mathbf{E}}_2 = E^{(2)}\hat{\mathbf{x}} = \mathbf{E}_2^{(+)} + \mathbf{E}_2^{(-)}$ , where we decompose the linear polarization into right and left circular polarization using the spherical basis:  $\hat{\mathbf{x}} = -\frac{1}{\sqrt{2}}\hat{\boldsymbol{\sigma}}^+ + \frac{1}{\sqrt{2}}\hat{\boldsymbol{\sigma}}^-$ . Likewise, we have  $\tilde{\mathbf{E}}_3 = E^{(3)}\hat{\mathbf{z}} = \mathbf{E}_3^{(m)}$  with  $\hat{\mathbf{z}} = \hat{\boldsymbol{\pi}}$ . Therefore, the spherical basis components of the fields used in the main text are

$$\mathbf{E}_{1}^{(\pm)} = \mp \frac{1}{\sqrt{2}} E^{(1)} \hat{\boldsymbol{\sigma}}^{\pm} \tag{D60}$$

$$\mathbf{E}_{2}^{(\pm)} = \mp \frac{1}{\sqrt{2}} E^{(2)} \hat{\boldsymbol{\sigma}}^{\pm}$$
 (D61)

$$\mathbf{E}_{3}^{(\pi)} = E^{(3)}\hat{\boldsymbol{\pi}}$$
 (D62)

Furthermore, we define  $\Omega_i$  as the couplings between *spherical* basis states, as shown in Fig. 1(b) in the main text,

$$\Omega_1 \equiv \frac{1}{\hbar} \langle^3 \mathbf{P}_1, m = 1 | \hat{\boldsymbol{\mu}} \cdot \mathbf{E}_1^{(+)} | ^1 \mathbf{S}_0 \rangle$$
(D63)

$$\Omega_2 \equiv \frac{1}{\hbar} \langle {}^3S_1, m = 0 | \hat{\boldsymbol{\mu}} \cdot \mathbf{E}_2^{(-)} | {}^3P_1, m = 1 \rangle$$
 (D64)

$$\Omega_3 \equiv \frac{1}{\hbar} \langle^3 \mathbf{P}_0 | \, \hat{\boldsymbol{\mu}} \cdot \mathbf{E}_3^{(\pi)} \, |^3 \mathbf{S}_1, m = 0 \rangle \tag{D65}$$

The states represented in the spherical basis are

$$|^{3}\mathbf{P}_{1}, m = 1\rangle = a ||^{3}\mathbf{P}_{1}^{(0)}|\rangle |J = 1, m = 1\rangle_{z} + b ||^{1}\mathbf{P}_{1}^{(0)}|\rangle |1, 1\rangle_{\ell} |0, 0\rangle_{s} |^{3}\mathbf{S}_{1}, m = 0\rangle = ||^{3}\mathbf{S}_{1}|\rangle |0, 0\rangle_{\ell} |1, 0\rangle_{s} |^{3}\mathbf{P}_{0}\rangle = ||^{3}\mathbf{P}_{0}|\rangle |J = 0, m = 0\rangle$$

and for transitions between these states, we have  $_{\ell}\langle 1,\pm 1|\,\hat{\boldsymbol{\mu}}\cdot\hat{\boldsymbol{\sigma}}^{\pm}\,|0,0\rangle_{\ell}=\hat{\mu}$  and  $_{\ell}\langle 1,0|\,\hat{\boldsymbol{\mu}}\cdot\hat{\boldsymbol{\pi}}\,|0,0\rangle_{\ell}=\hat{\mu}$ , for circularly polarized  $\sigma^{\pm}$  and  $\pi$  light, respectively. Evaluating the first

single-photon coupling in the spherical basis yields

$$\Omega_{1} = \frac{b^{*}}{\hbar} \langle |^{1} P_{1}^{(0)}| |_{\ell} \langle 1, 1|_{s} \langle 0, 0| \hat{\boldsymbol{\mu}} \cdot \mathbf{E}_{1}^{(+)} ||^{1} S_{0}| \rangle |0, 0\rangle_{\ell} |0, 0\rangle_{s} 
= \frac{b^{*}}{\hbar} \left( -\frac{1}{\sqrt{2}} E^{(1)} \right) \langle |^{1} P_{1}^{(0)}| |_{\ell} \langle 1, 1| \hat{\boldsymbol{\mu}} \cdot \hat{\boldsymbol{\sigma}}^{+} |0, 0\rangle_{\ell} ||^{1} S_{0}| \rangle 
= -\frac{b^{*} E^{(1)}}{\sqrt{2} \hbar} \langle |^{1} P_{1}^{(0)}| |\hat{\boldsymbol{\mu}}| ||^{1} S_{0}| \rangle$$
(D66)

Likewise, for the second coupling we have

$$\Omega_{2} = \frac{a}{\hbar} \langle |^{3} S_{1}||_{\ell} \langle 0, 0|_{s} \langle 1, 0|\hat{\boldsymbol{\mu}} \cdot \mathbf{E}_{2}^{(-)}||^{3} \mathbf{P}_{1}^{(0)}|\rangle |J = 1, m = 1 \rangle_{z} 
= \frac{aE^{(2)}}{2\hbar} \langle |^{3} S_{1}||_{\ell} \langle 0, 0|_{s} \langle 1, 0|\hat{\boldsymbol{\mu}} \cdot \hat{\boldsymbol{\sigma}}^{-}|1, 1 \rangle_{\ell} |1, 0 \rangle_{s} ||^{3} \mathbf{P}_{1}^{(0)}|\rangle 
= \frac{aE^{(2)}}{2\hbar} \langle |^{3} S_{1}||\hat{\mu}||^{3} \mathbf{P}_{1}^{(0)}|\rangle$$
(D67)

where in the second line we used Eq. (D40). Finally,

$$\Omega_{3} = \frac{1}{\hbar} \langle |^{3} P_{0}| | \langle J = 0, m = 0 | \hat{\boldsymbol{\mu}} \cdot \mathbf{E}_{3}^{(\pi)} | |^{3} S_{1} | \rangle |0, 0\rangle_{\ell} |1, 0\rangle_{s} 
= \frac{-E^{(3)}}{\sqrt{3}\hbar} \langle |^{3} P_{0}| |_{\ell} \langle 1, 0 |_{s} \langle 1, 0 | \hat{\boldsymbol{\mu}} \cdot \hat{\boldsymbol{\pi}} |0, 0\rangle_{\ell} |1, 0\rangle_{s} ||^{3} S_{1} | \rangle 
= -\frac{E^{(3)}}{\sqrt{3}\hbar} \langle |^{3} P_{0}| |\hat{\mu}| |^{3} S_{1} | \rangle$$
(D68)

where in the second line we used Eq.(D47). We can now write the matrix elements between the Cartesian states (Eq.(D59)) in terms of the single-photon Rabi couplings:

$$\langle {}^{3}\mathrm{P}_{1}, J_{n} | \hat{\boldsymbol{\mu}} \cdot \widetilde{\mathbf{E}}_{1}^{*} | {}^{1}\mathrm{S}_{0} \rangle = -\sqrt{2}\hbar \Omega_{1} (e_{n}^{(1)})^{*}$$
 (D69)

$$\langle {}^{3}\mathrm{S}_{1}, J_{l} | \, \hat{\boldsymbol{\mu}} \cdot \widetilde{\mathbf{E}}_{2}^{*} | {}^{3}\mathrm{P}_{1}, J_{j} \rangle = i\sqrt{2}\hbar \,\Omega_{2} \sum_{k} \epsilon_{jkl} (e_{k}^{(2)})^{*} \tag{D70}$$

$$\langle {}^{3}\mathrm{P}_{0}|\,\hat{\boldsymbol{\mu}}\cdot\widetilde{\mathbf{E}}_{3}\,|{}^{3}\mathrm{S}_{1},J_{l}\rangle = \hbar\,\Omega_{3}e_{l}^{(3)} \tag{D71}$$

#### 5. The effective coupling in the Cartesian basis

Substituting the above matrix elements into Eq.(D36) yields the main result:

$$\Omega_{\text{eff}} = \frac{\Omega_1 \Omega_2 \Omega_3}{2\Delta_2} \sum_{n,j,k,l} \epsilon_{jkl} D_{jn} (e_n^{(1)})^* (e_k^{(2)})^* e_l^{(3)} \quad (D72)$$

where here and in the main text we drop the overall phase of the three-photon coupling and report only the magnitude. This reproduces Eq. (1) in the main text, assuming linearly polarized (real)  $e_i^{(\alpha)}$ . In this work, we use  $\mathbf{e}^{(1)} = \mathbf{e}^{(2)} = \hat{\mathbf{x}}$  and  $\mathbf{e}^{(3)} = \hat{\mathbf{z}}$ , so the three-photon Rabi frequency is

$$\begin{split} &\Omega_{\text{eff}} = \frac{\Omega_1 \Omega_2 \Omega_3}{2\Delta_2} \epsilon_{213} D_{21} \\ &= \frac{\Omega_1 \Omega_2 \Omega_3}{2\Delta_2} \frac{\delta \omega_B}{\Delta_1^2 - \delta \omega_B^2} \\ &= \frac{\Omega_1 \Omega_2 \Omega_3}{4\Delta_2} \left( \frac{1}{\Delta_1 - \delta \omega_B} - \frac{1}{\Delta_1 + \delta \omega_B} \right) \end{split} \tag{D73}$$

where on the second line we once again drop the overall phase. This matches Eq. (3) in the main text. In the absence of a magnetic field, the Zeeman shift  $\delta\omega_B$  is zero and the matrix  $D_{jn}$  is diagonal. Specifically, we have  $D_{jn}=\frac{1}{\Delta_1}\delta_{jn}$  which gives

$$\Omega_{\text{eff}}(\mathbf{B} = 0) = \frac{\Omega_1 \Omega_2 \Omega_3}{2\Delta_1 \Delta_2} \sum_{j,k,l} \epsilon_{jkl} (e_j^{(1)})^* (e_k^{(2)})^* e_l^{(3)} 
= \frac{\Omega_1 \Omega_2 \Omega_3}{2\Delta_1 \Delta_2} \left[ (\mathbf{e}^{(2)})^* \times \mathbf{e}^{(3)} \right] \cdot (\mathbf{e}^{(1)})^* \quad (D74)$$

In the case of linear polarization, we recover Eq. (2) from the main text:

$$\Omega_{\text{eff}}(\mathbf{B} = 0) = \frac{\Omega_1 \Omega_2 \Omega_3}{2\Delta_1 \Delta_2} \, \mathbf{e}^{(1)} \cdot \left( \mathbf{e}^{(2)} \times \mathbf{e}^{(3)} \right) \qquad (D75)$$

This shows that with no magnetic field,  $\Omega_{\rm eff}$  is proportional to the volume spanned by the three  ${\bf e}^{(i)}$  vectors. When all three vectors are mutually orthogonal, the coupling is  $\Omega_0 \equiv \Omega_1\Omega_2\Omega_3/(2\Delta_1\Delta_2)$ , which corresponds to the maximum Rabi frequency. In this limit, it is not possible to have all three light fields collinear, because in that case the volume spanned is zero.

## 6. Effective wave function of the <sup>3</sup>P<sub>1</sub> state

In Fig. 2 in the main text, we visualize the three-photon coupling in terms of the three sequential single-photon couplings linking  $^1S_0,\ ^3P_1,\ ^3S_1,\$ and  $^3P_0.$  The effect of the magnetic field on the coupling can be understood by defining an effective wavefunction that couples to  $|^3S_1\rangle$  as it appears in Eq. (D36)

$$|\psi(\theta_B)\rangle \equiv \frac{1}{N} \sum_{j,n} |^3 \mathbf{P}_1, J_j\rangle D_{jn} \langle ^3 \mathbf{P}_1, J_n | \, \hat{\boldsymbol{\mu}} \cdot \widetilde{\mathbf{E}}_1^* \, |^1 \mathbf{S}_0 \rangle$$
$$= \frac{\sqrt{2}\hbar\Omega_1}{N} \sum_j |^3 \mathbf{P}_1, J_j\rangle D_{j1}$$
(D76)

where N is a normalization factor and we have substituted in the definition of  $\Omega_1$  from Eq. (D69) with  $\mathbf{e}^{(1)} = \hat{\mathbf{x}}$ . With this definition, Eq. (D36) has the form of a two-photon transition from  $|\psi(\theta_B)\rangle$  to  $|^3P_0\rangle$ , i.e.

$$\Omega_{\text{eff}} = N \sum_{l} \frac{\langle^{3} \mathbf{P}_{0} | \, \hat{\boldsymbol{\mu}} \cdot \widetilde{\mathbf{E}}_{3} \, |^{3} \mathbf{S}_{1}, J_{l} \rangle \, \langle^{3} \mathbf{S}_{1}, J_{l} | \, \hat{\boldsymbol{\mu}} \cdot \widetilde{\mathbf{E}}_{2}^{*} \, | \psi(\theta_{B}) \rangle}{4 \Delta_{2} \hbar^{3}} \tag{D77}$$

To obtain an explicit expression for  $|\psi(\theta_B)\rangle$ , we define the dimensionless parameter  $\beta \equiv \delta\omega_B/\Delta_1$  so that  $D_{jn}$  from Eq. (D35) becomes

$$D_{jn} \doteq \frac{1}{\Delta_1} \begin{pmatrix} \frac{1}{1-\beta^2} & -\frac{i\beta}{1-\beta^2} & 0\\ \frac{i\beta}{1-\beta^2} & \frac{1}{1-\beta^2} & 0\\ 0 & 0 & 1 \end{pmatrix}$$
 (D78)

Although  $\Omega_{\rm eff}$  is nonzero for j=n=3, this case requires noncollinear light fields and gives a coupling strength that is identical to the  ${\bf B}=0$  case, independent of the magnetic field. Thus, with minimal loss of generality, we neglect this case and consider only the upper left  $2\times 2$  part of the matrix:

$$D_{jn} \doteq \frac{1}{\Delta_1} \begin{pmatrix} d_{jn} & 0 \\ \hline 0 & 0 & 1 \end{pmatrix} \quad d_{jn} \doteq \begin{pmatrix} \frac{1}{1-\beta^2} & -\frac{i\beta}{1-\beta^2} \\ \frac{i\beta}{1-\beta^2} & \frac{1}{1-\beta^2} \end{pmatrix}$$
(D79)

Further defining  $\theta_B \equiv \arctan \beta$ , the matrix  $d_{jn}$  becomes

$$d_{jn} \doteq \frac{\sqrt{1+\beta^2}}{1-\beta^2} \begin{pmatrix} \cos \theta_B & -i\sin \theta_B \\ i\sin \theta_B & \cos \theta_B \end{pmatrix}$$
 (D80)

After we impose the above restriction to the interesting case where the polarization  $\mathbf{e}^{(1)}$  lies in the plane perpendicular to  $\mathbf{B}$ , we are free to orient our coordinate system such that the first laser is polarized along  $\hat{\mathbf{x}}$ . Thus, without further loss of generality we choose  $\mathbf{e}^{(1)} = \hat{\mathbf{x}}$ . With this, the sum in Eq. (D76) reduces to a sum over  $d_{j1}$ , and for the normalization factor N we find

$$N = \frac{\sqrt{2}\hbar\Omega_1}{\Delta_1} \frac{\sqrt{1+\beta^2}}{1-\beta^2}$$
 (D81)

The effective wave function is then

$$|\psi(\theta_B)\rangle = a \left| \left| {}^{3}P_1^{(0)} \right| \rangle \left( \cos \theta_B \left| J_x \right\rangle + i \sin \theta_B \left| J_y \right\rangle \right) + b \left| \left| {}^{1}P_1^{(0)} \right| \rangle \left( \cos \theta_B \left| L_x \right\rangle + i \sin \theta_B \left| L_y \right\rangle \right) |0, 0\rangle_s$$

where we used Eq. (D38) and Eq. (D39) to express the result in terms of the triplet and singlet parts. Here  $|\big|^3P_1^{(0)}\big|\rangle$  and  $|\big|^1P_1^{(0)}\big|\rangle$  are the radial parts of the triplet and singlet components, respectively. As we will see below, only the triplet component of  $|\psi(\theta_B)\rangle$  ultimately contributes to the three-photon coupling since the other atomic states are orthogonal to  $|0,0\rangle_s$ . We define the angular parts of the effective wave function as

$$|^{3}P_{1}, \theta_{B}\rangle \equiv \cos \theta_{B} |J_{x}\rangle + i \sin \theta_{B} |J_{y}\rangle$$
 (D82)

$$|^{1}P_{1}, \theta_{B}\rangle \equiv (\cos \theta_{B} | L_{x}\rangle + i \sin \theta_{B} | L_{y}\rangle) |0, 0\rangle$$
 (D83)

resulting in

$$|\psi(\theta_B)\rangle = a \left| \left| {}^{3}\mathbf{P}_{1}^{(0)} \right| \right\rangle \left| {}^{3}\mathbf{P}_{1}, \theta_B \right\rangle + b \left| \left| {}^{1}\mathbf{P}_{1}^{(0)} \right| \right\rangle \left| {}^{1}\mathbf{P}_{1}, \theta_B \right\rangle \tag{D84}$$

Focusing on the triplet component, we decompose  $|^{3}P_{1}, \theta_{B}\rangle$  in terms of **L** and **S** using Eq. (D43):

$$|^{3}P_{1}, \theta_{B}\rangle = \frac{1}{\sqrt{2}} \left( \sin \theta_{B} |L_{x}\rangle + i \cos \theta_{B} |L_{y}\rangle \right) |S_{z}\rangle - \frac{1}{\sqrt{2}} |L_{z}\rangle \left( \sin \theta_{B} |S_{x}\rangle + i \cos \theta_{B} |S_{y}\rangle \right)$$
(D85)

This corresponds to Eq. (4) in the main text.

In Fig. 2 in the main text, we show the angular wave function of each of the atomic states that determine the sequential single-photon couplings in Eq. (D36), with color indicating the spin state. For a particular state  $|\psi\rangle$ , we plot the probability density  $f_n(\theta,\phi)=|\langle S_n,\mathbf{r}|\psi\rangle|^2$  for each spin projection. We choose to represent the different spin states using color according to  $f_0(\theta,\phi)=|\langle S=0,\mathbf{r}|\psi\rangle|^2$  (gray) for S=0, and  $\{f_x$  (red),  $f_y$  (green),  $f_z$  (blue) $\}$  for S=1. The position-space representations of the Cartesian basis states  $\langle \mathbf{r}|L_n\rangle$  follow from Eqs. (D29) to (D31):

$$\begin{split} \langle \mathbf{r}|L=0\rangle &= Y_{0,0} \\ \langle \mathbf{r}|L_x\rangle &= -\frac{1}{\sqrt{2}} \left(Y_{1,+1} - Y_{1,-1}\right) \\ \langle \mathbf{r}|L_y\rangle &= -\frac{1}{i\sqrt{2}} \left(Y_{1,+1} + Y_{1,-1}\right) \\ \langle \mathbf{r}|L_z\rangle &= Y_{1,0} \end{split}$$

where  $Y_{\ell,m}(\theta,\phi)$  are the spherical harmonics.

The  $^1\mathrm{S}_0$  state has L=0 and S=0, resulting in a spherically symmetric s orbital colored gray according to our convention. Next, the angular wave function in Eq. (D85) describes the triplet component of the  $^3\mathrm{P}_1$  state (assuming  $\mathbf{e}^{(1)} = \hat{\mathbf{x}}$ , as above) as a function of  $\theta_B$ , resulting in the following spin components

$$f_x(\theta, \phi) = \frac{1}{2} \sin^2 \theta_B |Y_{1,0}|^2$$

$$f_y(\theta, \phi) = \frac{1}{2} \cos^2 \theta_B |Y_{1,0}|^2$$

$$f_z(\theta, \phi) = \frac{1}{4} \left( \sin^2 \theta_B |Y_{1,+1} - Y_{1,-1}|^2 + \cos^2 \theta_B |Y_{1,+1} + Y_{1,-1}|^2 \right)$$

Note that the  $f_x$  and  $f_y$  components here both have the shape of a  $p_z$  orbital, and so the color interpolates between green and red as a function of  $\theta_B$  in our visualization. Figure 2 in the main text omits the singlet component of  ${}^3P_1$  that appears in Eq. (D84) for the practical reason that  $|b|^2 \ll |a|^2$ , and also because only the triplet component is coupled by the 688 nm transition. The  ${}^3S_1$  state has L=0 and S=1, and so it appears as a spherically symmetric s orbital whose color depends on the  $|S_n\rangle$  state of the excitation pathway. Finally, the Cartesian basis representation of  $|{}^3P_0\rangle$  is given by Eq. (D49), resulting in spin components

$$f_x(\theta,\phi) = \frac{1}{6}|Y_{1,+1} - Y_{1,-1}|^2$$
  
$$f_y(\theta,\phi) = \frac{1}{6}|Y_{1,+1} + Y_{1,-1}|^2$$
  
$$f_z(\theta,\phi) = \frac{1}{2}|Y_{1,0}|^2$$

which have the shape of a  $p_x$ ,  $p_y$ , and  $p_z$  orbital, respectively.

## 7. Parameterizations of the three-photon coupling

In terms of the dimensionless detuning  $\beta \equiv \delta \omega_B/\Delta_1$ , the three-photon coupling in Eq. (D73) is

$$\Omega_{\text{eff}} = \Omega_0 \, \frac{\beta}{1 - \beta^2} \tag{D86}$$

matching Eq. (6) in the main text. This can also be written in terms of the projection angle  $\theta_B$ . Starting from Eq. (D77), we use Eq. (D84) to express the coupling in terms of the angular part of the effective  ${}^3P_1$  wave function:

$$\Omega_{\text{eff}} = Na \sum_{l} \frac{\langle^{3} P_{0} | \hat{\boldsymbol{\mu}} \cdot \widetilde{\mathbf{E}}_{3} |^{3} S_{1}, J_{l} \rangle \langle^{3} S_{1}, J_{l} | \hat{\boldsymbol{\mu}} \cdot \widetilde{\mathbf{E}}_{2}^{*} | |^{3} P_{1}^{(0)} | \rangle |^{3} P_{1}, \theta_{B} \rangle}{4 \Delta_{2} \hbar^{3}}$$
(D87)

where only the triplet component of the effective wave function contributes since  $\langle {}^3{\rm S}_1,J_l|$  is orthogonal to the singlet part of  $|\psi(\theta_B)\rangle$ . In the experiment, we used polarizations  $\hat{\bf x}-\hat{\bf x}-\hat{\bf z}$ . Assuming  ${\bf e}^{(3)}=\hat{\bf z}$ , the sum over l collapses to l=3 and picks out the  $|J_z\rangle$  term:

$$\Omega_{\text{eff}} = \frac{Na\Omega_3}{4\Delta_2\hbar^2} \langle {}^3S_1, J_z | \, \hat{\boldsymbol{\mu}} \cdot \widetilde{\mathbf{E}}_2^* \, | \, |^3P_1^{(0)} | \rangle \, |^3P_1, \theta_B \rangle \quad (D88)$$

where we use  $\Omega_3$  as defined in Eq. (D71). For  $\mathbf{E}_2$ , we allow a more general elliptical polarization:

$$\mathbf{e}^{(2)} = \sin\theta \,\hat{\mathbf{x}} + i\cos\theta \,\hat{\mathbf{y}} \tag{D89}$$

where  $\theta$  is the ellipticity angle and we have restricted the polarization to the xy-plane in order to be orthogonal to  $\mathbf{e}^{(3)} = \hat{\mathbf{z}}$ , as is required to maximize the coupling. As noted in the main text,  $\theta = \pi/2$  is the only choice for  $\mathbf{e}^{(2)}$  that is compatible with collinear propagation along  $\hat{\mathbf{y}}$ . In the more general case, we therefore have

$$\hat{\boldsymbol{\mu}} \cdot \tilde{\mathbf{E}}_2^* = E^{(2)} \Big( \sin \theta \, \hat{\mu}_x - i \cos \theta \, \hat{\mu}_y \Big)$$
 (D90)

which then gives

$$\Omega_{\text{eff}} = \frac{Na E^{(2)} \Omega_3}{4 \Delta_2 \hbar^2} \left\langle \left| {}^3S_1 \right| \left| \left\langle S_z \right|_{\ell} \left\langle 0, 0 \right| \left( \sin \theta \, \hat{\mu}_x - i \cos \theta \, \hat{\mu}_y \right) \left| \left| {}^3P_1^{(0)} \right| \right\rangle \left| {}^3P_1, \theta_B \right\rangle \right.$$
(D91)

where we used Eq. (D46). From Eq. (D58), we have  $\hat{\mu}_n |0,0\rangle_{\ell} = \hat{\mu} |L_n\rangle$  in general, which implies

$$\Omega_{\text{eff}} = \frac{Na E^{(2)} \Omega_3}{4 \Delta_2 \hbar^2} \left\langle \left| {}^3 S_1 \right| \left| \hat{\mu} \right| \left| {}^3 P_1^{(0)} \right| \right\rangle \left\langle S_z \right| \left( \sin \theta \left\langle L_x \right| - i \cos \theta \left\langle L_y \right| \right) \left| {}^3 P_1, \theta_B \right\rangle. \tag{D92}$$

Using Eq. (D67) for the dipole matrix element,

$$\Omega_{\text{eff}} = \frac{N\Omega_2\Omega_3}{2\Delta_2\hbar} \langle S_z | \langle L, \theta | |^3 P_1, \theta_B \rangle$$
 (D93)

where we have defined

$$\langle L, \theta | \equiv \sin \theta \langle L_x | -i \cos \theta \langle L_y |.$$
 (D94)

Inserting the normalization factor N, we find

$$\Omega_{\text{eff}} = \sqrt{2} \Omega_0 \frac{\sqrt{1+\beta^2}}{1-\beta^2} \langle S_z | \langle L, \theta | |^3 P_1, \theta_B \rangle 
= \sqrt{2} \Omega_B \langle S_z | \langle L, \theta | |^3 P_1, \theta_B \rangle$$
(D95)

where  $\Omega_B \equiv \Omega_0 \sqrt{1+\beta^2}/(1-\beta^2)$ . Thus we see that the three-photon coupling is proportional to the projection of the effective wave function  $|{}^3P_1, \theta_B\rangle$  onto a vector  $\langle S_z | \langle L, \theta |$  determined by the light polarization ellipticity angle  $\theta$ .

Using Eq. (D85),

$$\langle S_z | \langle L, \theta | |^3 P_1, \theta_B \rangle = \frac{1}{\sqrt{2}} (\sin \theta \sin \theta_B + \cos \theta \cos \theta_B)$$

and so we have

$$\Omega_{\text{eff}} = \Omega_B \cos(\theta_B - \theta).$$
 (D96)

This shows that the coupling depends on the relative alignment of the atom's effective dipole moment (as determined by  $\theta_B$ ) with the polarization of the light (as set by  $\theta$ ). The magnetic field tunes this dipole moment in much the same way as a wave plate rotates the polarization of light. Finally, when we restrict to the case  $\theta = \pi/2$  as we assume in the main text, we have

$$\Omega_{\text{eff}} = \Omega_B \sin \theta_B \tag{D97}$$

which reproduces Eq. (7) in the main text.

- [1] H. Katori, *Optical lattice clocks and quantum metrology*, Nat. Photon. **5**, 203–210 (2011).
- [2] M. G. Kozlov, M. S. Safronova, J. R. Crespo López-Urrutia, and P. O. Schmidt, *Highly charged ions: Optical clocks and ap*plications in fundamental physics, Rev. Mod. Phys. **90**, 045005 (2018).
- [3] J. Grotti, S. Koller, S. Vogt, S. Haefner, U. Sterr, C. Lisdat, H. Denker, C. Voigt, L. Timmen, A. Rolland, F. Baynes, H. Margolis, M. Zampaolo, P. Thoumany, M. Pizzocaro, B. Rauf, F. Bregolin, A. Tampellini, P. Barbieri, and D. Calonico, Geodesy and metrology with a transportable optical clock, Nat. Phys. 14, 437–441 (2018).
- [4] B. J. Bloom, T. L. Nicholson, J. R. Williams, S. L. Campbell, M. Bishof, X. Zhang, W. Zhang, S. L. Bromley, and J. Ye, An optical lattice clock with accuracy and stability at the 10<sup>-18</sup> level, Nature 506, 71 (2014).
- [5] A. D. Ludlow, M. M. Boyd, J. Ye, E. Peik, and P. O. Schmidt, Optical atomic clocks, Rev. Mod. Phys. 87, 637–701 (2015).
- [6] G. E. Marti, R. B. Hutson, A. Goban, S. L. Campbell, N. Poli, and J. Ye, *Imaging Optical Frequencies with* 100 µHz *Precision and* 1.1 µm *Resolution*, Phys. Rev. Lett. 120, 103201 (2018).
- [7] S. Blatt, A. D. Ludlow, G. K. Campbell, J. W. Thomsen, T. Zelevinsky, M. M. Boyd, J. Ye, X. Baillard, M. Fouché, R. Le Targat, A. Brusch, P. Lemonde, M. Takamoto, F.-L. Hong, H. Katori, and V. V. Flambaum, New Limits on Coupling of Fundamental Constants to Gravity Using <sup>87</sup>Sr Optical Lattice Clocks, Phys. Rev. Lett. 100, 140801 (2008).
- [8] R. M. Godun, P. B. R. Nisbet-Jones, J. M. Jones, S. A. King, L. A. M. Johnson, H. S. Margolis, K. Szymaniec, S. N. Lea, K. Bongs, and P. Gill, Frequency Ratio of Two Optical Clock

- Transitions in <sup>171</sup>Yb<sup>+</sup> and Constraints on the Time Variation of Fundamental Constants, Phys. Rev. Lett. **113**, 210801 (2014).
- [9] M. Takamoto, I. Ushijima, N. Ohmae, T. Yahagi, K. Kokado, H. Shinkai, and H. Katori, *Test of general relativity by a pair of transportable optical lattice clocks*, Nat. Photon. 14, 411–415 (2020).
- [10] T. Bothwell, C. J. Kennedy, A. Aeppli, D. Kedar, J. M. Robinson, E. Oelker, A. Staron, and J. Ye, Resolving the gravitational redshift across a millimetre-scale atomic sample, Nature 602, 420–424 (2022).
- [11] T. Bothwell, D. Kedar, E. Oelker, J. Robinson, S. Bromley, W. Tew, J. Ye, and C. Kennedy, *JILA* Sr I *optical lattice clock with uncertainty of*  $2.0 \times 10^{-18}$ , Metrologia **56** (2019).
- [12] W. F. McGrew, X. Zhang, R. J. Fasano, S. A. Schäffer, K. Beloy, D. Nicolodi, R. C. Brown, N. Hinkley, G. Milani, M. Schioppo, T. H. Yoon, and A. D. Ludlow, *Atomic clock performance* enabling geodesy below the centimetre level, Nature **564**, 87–90 (2018).
- [13] A. P. Kulosa, D. Fim, K. H. Zipfel, S. Rühmann, S. Sauer, N. Jha, K. Gibble, W. Ertmer, E. M. Rasel, M. S. Safronova, U. I. Safronova, and S. G. Porsev, *Towards a Mg Lattice Clock: Observation of the* <sup>1</sup>S<sub>0</sub> - <sup>3</sup>P<sub>0</sub> *Transition and Determination of the Magic Wavelength*, Phys. Rev. Lett. **115**, 240801 (2015).
- [14] S. M. Brewer, J.-S. Chen, A. M. Hankin, E. R. Clements, C. W. Chou, D. J. Wineland, D. B. Hume, and D. R. Leibrandt, <sup>27</sup>Al<sup>+</sup> *Quantum-Logic Clock with a Systematic Uncertainty below* 10<sup>-18</sup>, Phys. Rev. Lett. **123**, 033201 (2019).
- [15] A. V. Taichenachev, V. I. Yudin, C. W. Oates, C. W. Hoyt, Z. W. Barber, and L. Hollberg, Magnetic Field-Induced Spectroscopy of Forbidden Optical Transitions with Application to Lattice-

- Based Optical Atomic Clocks, Phys. Rev. Lett. 96, 083001 (2006).
- [16] Z. W. Barber, C. W. Hoyt, C. W. Oates, L. Hollberg, A. V. Taichenachev, and V. I. Yudin, *Direct excitation of the forbidden clock transition in neutral* <sup>174</sup>Yb atoms confined to an optical lattice, Phys. Rev. Lett. **96**, 083002 (2006).
- [17] T. Akatsuka, M. Takamoto, and H. Katori, Optical lattice clocks with non-interacting bosons and fermions, Nat. Phys. 4, 954–959 (2008).
- [18] N. Poli, M. Schioppo, S. Vogt, S. Falke, U. Sterr, C. Lisdat, and G. M. Tino, A transportable strontium optical lattice clock, Appl. Phys. B. 117, 1107 – 1116 (2014).
- [19] R. Santra, E. Arimondo, T. Ido, C. H. Greene, and J. Ye, High-Accuracy Optical Clock via Three-Level Coherence in Neutral Bosonic <sup>88</sup>Sr, Phys. Rev. Lett. 94, 173002 (2005).
- [20] T. Hong, C. Cramer, W. Nagourney, and E. N. Fortson, Optical Clocks Based on Ultranarrow Three-Photon Resonances in Alkaline Earth Atoms, Phys. Rev. Lett. 94, 050801 (2005).
- [21] V. D. Ovsiannikov, V. G. Pal'chikov, A. V. Taichenachev, V. I. Yudin, H. Katori, and M. Takamoto, *Magic-wave-induced* <sup>1</sup>S<sub>0</sub> <sup>3</sup> P<sub>0</sub> transition in even isotopes of alkaline-earth-metallike atoms, Phys. Rev. A **75**, 020501(R) (2007).
- [22] E. A. Alden, K. R. Moore, and A. E. Leanhardt, *Two-photon E1-M1 optical clock*, Phys. Rev. A **90**, 012523 (2014).
- [23] D. S. Barker, N. C. Pisenti, B. J. Reschovsky, and G. K. Campbell, *Three-photon process for producing a degenerate gas of metastable alkaline-earth-metal atoms*, Phys. Rev. A 93, 053417 (2016).
- [24] G. Grynberg, B. Cagnac, and F. Biraben, *Multiphoton Resonant Processes in Atoms*, in *Coherent Nonlinear Optics: Recent Advances* (Springer, 1980) pp. 111–164.
- [25] G. Panelli, S. C. Burd, E. J. Porter, and M. Kasevich, *Doppler-free three-photon spectroscopy on narrow-line optical transitions*, Phys. Rev. A 111, 033112 (2025).
- [26] I. S. Madjarov, J. P. Covey, A. L. Shaw, J. Choi, A. Kale, A. Cooper, H. Pichler, V. Schkolnik, J. R. Williams, and M. Endres, *High-fidelity entanglement and detection of alkaline-earth Rydberg atoms*, Nat. Phys. 16, 857 (2020).
- [27] N. Schine, A. Young, W. Eckner, M. Martin, and A. Kaufman, Long-lived Bell states in an array of optical clock qubits, Nat. Phys. 18 (2022).
- [28] W. Eckner, N. Oppong, A. Cao, A. Young, W. Milner, J. Robinson, J. Ye, and A. Kaufman, *Realizing spin squeezing with Rydberg interactions in an optical clock*, Nature 621, 734–739 (2023).
- [29] A. Cao, W. J. Eckner, T. L. Yelin, A. W. Young, S. Jandura, L. Yan, K. Kim, G. Pupillo, J. Ye, N. D. Oppong, and A. M. Kaufman, *Multi-qubit gates and 'Schrödinger cat' states in an optical clock*, Nature 634, 315–320 (2024).
- [30] N. Hinkley, J. A. Sherman, N. B. Phillips, M. Schioppo, N. D. Lemke, K. Beloy, M. Pizzocaro, C. W. Oates, and A. D. Ludlow, An Atomic Clock with 10<sup>-18</sup> Instability, Science 341, 1215–1218 (2013).
- [31] S. Kolkowitz, I. Pikovski, N. Langellier, M. D. Lukin, R. L. Walsworth, and J. Ye, *Gravitational wave detection with optical lattice atomic clocks*, Phys. Rev. D 94, 124043 (2016).
- [32] M. Schioppo, R. Brown, W. McGrew, N. Hinkley, R. Fasano, K. Beloy, T. H. Yoon, G. Milani, D. Nicolodi, J. Sherman, N. Phillips, C. Oates, and A. Ludlow, *Ultra-stable optical clock* with two cold-atom ensembles, Nat. Photon. 11, 48–52 (2016).
- [33] E. Oelker, R. Hutson, C. Kennedy, L. Sonderhouse, T. Bothwell, A. Goban, D. Kedar, C. Sanner, J. Robinson, G. Marti, D. Matei, T. Legero, M. Giunta, R. Holzwarth, F. Riehle, U. Sterr, and

- J. Ye, Demonstration of  $4.8 \times 10^{-17}$  stability at 1 s for two independent optical clocks, Nat. Photon. 13 (2019).
- [34] Boulder Atomic Clock Optical Network (BACON) Collaboration, Frequency ratio measurements at 18-digit accuracy using an optical clock network, Nature 591, 564–569 (2021).
- [35] X. Zheng, J. Dolde, V. Lochab, B. Merriman, H. Li, and S. Kolkowitz, *Differential clock comparisons with a multiplexed optical lattice clock*, Nature 602, 425–430 (2022).
- [36] L. Hu, N. Poli, L. Salvi, and G. M. Tino, Atom Interferometry with the Sr Optical Clock Transition, Phys. Rev. Lett. 119, 263601 (2017).
- [37] M. Abe, P. Adamson, M. Borcean, D. Bortoletto, K. Bridges, S. P. Carman, S. Chattopadhyay, J. Coleman, N. M. Curfman, K. DeRose, T. Deshpande, S. Dimopoulos, C. J. Foot, J. C. Frisch, B. E. Garber, S. Geer, V. Gibson, J. Glick, P. W. Graham, S. R. Hahn, R. Harnik, L. Hawkins, S. Hindley, J. M. Hogan, Y. Jiang, M. A. Kasevich, R. J. Kellett, M. Kiburg, T. Kovachy, J. D. Lykken, J. March-Russell, J. Mitchell, M. Murphy, M. Nantel, L. E. Nobrega, R. K. Plunkett, S. Rajendran, J. Rudolph, N. Sachdeva, M. Safdari, J. K. Santucci, A. G. Schwartzman, I. Shipsey, H. Swan, L. R. Valerio, A. Vasonis, Y. Wang, and T. Wilkason, Matter-wave Atomic Gradiometer Interferometric Sensor (MAGIS-100), Quantum Sci. Technol. 6, 044003 (2021).
- [38] P. W. Graham, J. M. Hogan, M. A. Kasevich, and S. Rajendran, New Method for Gravitational Wave Detection with Atomic Sensors, Phys. Rev. Lett. 110, 171102 (2013).
- [39] Though we only show the case where the first photon is  $\hat{\mathbf{x}}$  polarized, the requirement for noncoplanar polarizations is independent of the choice of the first polarization for any  $\mathbf{e}^{(1)} \perp \mathbf{B}$ .
- [40] M. A. Kasevich and S. Chu, Atomic interferometry using stimulated Raman transitions, Phys. Rev. Lett. 67, 181–184 (1991).
- [41] L. Hu, E. Wang, L. Salvi, J. N. Tinsley, G. M. Tino, and N. Poli, Sr atom interferometry with the optical clock transition as a gravimeter and a gravity gradiometer, Class. Quantum Grav. 37, 014001 (2019).
- [42] J. Hartwig, S. Abend, C. Schubert, D. Schlippert, H. Ahlers, K. Posso-Trujillo, N. Gaaloul, W. Ertmer, and E. M. Rasel, Testing the universality of free fall with rubidium and ytterbium in a very large baseline atom interferometer, New J. Phys. 17, 035011 (2015).
- [43] T. Kovachy, P. Asenbaum, C. Overstreet, C. A. Donnelly, S. M. Dickerson, A. Sugarbaker, J. M. Hogan, and M. A. Kasevich, *Quantum superposition at the half-metre scale*, Nature 528, 530 (2015).
- [44] J. A. Muniz, D. J. Young, J. R. K. Cline, and J. K. Thompson, Cavity-QED measurements of the <sup>87</sup>Sr millihertz optical clock transition and determination of its natural linewidth, Phys. Rev. Res. 3, 023152 (2021).
- [45] V. Xu, M. Jaffe, C. D. Panda, S. L. Kristensen, L. W. Clark, and H. Müller, *Probing gravity by holding atoms for 20 seconds*, Science 366, 745–749 (2019).
- [46] T. Wilkason, M. Nantel, J. Rudolph, Y. Jiang, B. E. Garber, H. Swan, S. P. Carman, M. Abe, and J. M. Hogan, *Atom Interferometry with Floquet Atom Optics*, Phys. Rev. Lett. 129, 183202 (2022).
- [47] J. Rudolph, T. Wilkason, M. Nantel, H. Swan, C. M. Holland, Y. Jiang, B. E. Garber, S. P. Carman, and J. M. Hogan, *Large Momentum Transfer Clock Atom Interferometry on the* 689 nm *Intercombination Line of Strontium*, Phys. Rev. Lett. 124, 083604 (2020).

- [48] S. S. Szigeti, J. E. Debs, J. J. Hope, N. P. Robins, and J. D. Close, Why momentum width matters for atom interferometry with Bragg pulses, New J. Phys. 14, 023009 (2012).
- [49] A. D. Cronin, J. Schmiedmayer, and D. E. Pritchard, *Optics and interferometry with atoms and molecules*, Rev. Mod. Phys. 81, 1051–1129 (2009).
- [50] L. Badurina, E. Bentine, D. Blas, K. Bongs, D. Bortoletto, T. Bowcock, K. Bridges, W. Bowden, O. Buchmueller, C. Burrage, J. Coleman, G. Elertas, J. Ellis, C. Foot, V. Gibson, M. Haehnelt, T. Harte, S. Hedges, R. Hobson, M. Holynski, T. Jones, M. Langlois, S. Lellouch, M. Lewicki, R. Maiolino, P. Majewski, S. Malik, J. March-Russell, C. McCabe, D. Newbold, B. Sauer, U. Schneider, I. Shipsey, Y. Singh, M. Uchida, T. Valenzuela, M. van der Grinten, V. Vaskonen, J. Vossebeld, D. Weatherill, and I. Wilmut, AION: an atom interferometer observatory and network, J. Cosmol. Astropart. Phys. 2020 (05), 011.
- [51] A. Béguin, T. Rodzinka, L. Calmels, B. Allard, and A. Gauguet, Atom Interferometry with Coherent Enhancement of Bragg Pulse Sequences, Phys. Rev. Lett. 131, 143401 (2023).
- [52] A. Dunning, R. Gregory, J. Bateman, N. Cooper, M. Himsworth, J. A. Jones, and T. Freegarde, *Composite pulses for interferom*etry in a thermal cold atom cloud, Phys. Rev. A 90, 033608 (2014).
- [53] X. Baillard, M. Fouché, R. Targat, P. Westergaard, A. Lecallier, Y. Le Coq, G. Rovera, S. Bize, and P. Lemonde, Accuracy Evaluation of an Optical Lattice Clock with Bosonic Atoms, Opt. Lett. 32, 1812–4 (2007).
- [54] T. Akatsuka, M. Takamoto, and H. Katori, *Three-dimensional optical lattice clock with bosonic* <sup>88</sup>Sr *atoms*, Phys. Rev. A 81, 023402 (2010).
- [55] S. Origlia, M. S. Pramod, S. Schiller, Y. Singh, K. Bongs, R. Schwarz, A. Al-Masoudi, S. Dörscher, S. Herbers, S. Häfner, U. Sterr, and C. Lisdat, *Towards an optical clock for space: Compact, high-performance optical lattice clock based on bosonic atoms*, Phys. Rev. A 98, 053443 (2018).
- [56] M. A. Norcia, A. W. Young, W. J. Eckner, E. Oelker, J. Ye, and A. M. Kaufman, Seconds-scale coherence on an optical clock transition in a tweezer array, Science 366, 93–97 (2019).
- [57] R. Stock, N. S. Babcock, M. G. Raizen, and B. C. Sanders, Entanglement of group-II-like atoms with fast measurement for quantum information processing, Phys. Rev. A 78, 022301 (2008).
- [58] A. Young, W. Eckner, W. Milner, D. Kedar, M. Norcia, E. Oelker, N. Schine, J. Ye, and A. Kaufman, *Half-minute-scale atomic coherence and high relative stability in a tweezer clock*, Nature 588, 408–413 (2020).
- [59] A. Pagano, S. Weber, D. Jaschke, T. Pfau, F. Meinert, S. Montangero, and H. P. Büchler, Error budgeting for a controlled-phase gate with strontium-88 Rydberg atoms, Phys. Rev. Res. 4, 033019 (2022).
- [60] D. Okuno, Y. Nakamura, T. Kusano, Y. Takasu, N. Takei, H. Konishi, and Y. Takahashi, High-resolution Spectroscopy and Single-photon Rydberg Excitation of Reconfigurable Ytterbium Atom Tweezer Arrays Utilizing a Metastable State, J. Phys. Soc. Jpn. 91, 084301 (2022).
- [61] J. Trautmann, D. Yankelev, V. Klüsener, A. J. Park, I. Bloch, and S. Blatt, <sup>1</sup>S<sub>0</sub>-<sup>3</sup>P<sub>2</sub> magnetic quadrupole transition in neutral strontium, Phys. Rev. Res. 5, 013219 (2023).
- [62] S. Pucher, V. Klüsener, F. Spriestersbach, J. Geiger, A. Schindewolf, I. Bloch, and S. Blatt, Fine-Structure Qubit Encoded in Metastable Strontium Trapped in an Optical Lattice, Phys. Rev. Lett. 132, 150605 (2024).

- [63] V. Klüsener, S. Pucher, D. Yankelev, J. Trautmann, F. Spriestersbach, D. Filin, S. G. Porsev, M. S. Safronova, I. Bloch, and S. Blatt, Long-Lived Coherence on a μHz Scale Optical Magnetic Quadrupole Transition, Phys. Rev. Lett. 132, 253201 (2024).
- [64] J. He, B. Pasquiou, R. G. Escudero, S. Zhou, M. Borkowski, and F. Schreck, Coherent three-photon excitation of the strontium clock transition, Phys. Rev. Res. 7, L012050 (2025).
- [65] G. Ferrari, P. Cancio, R. Drullinger, G. Giusfredi, N. Poli, M. Prevedelli, C. Toninelli, and G. M. Tino, *Precision Frequency Measurement of Visible Intercombination Lines of Strontium*, Phys. Rev. Lett. **91**, 243002 (2003).
- [66] T. L. Nicholson, S. L. Campbell, R. B. Hutson, G. E. Marti, B. J. Bloom, R. L. McNally, W. Zhang, M. D. Barrett, M. S. Safronova, G. F. Strouse, W. L. Tew, and J. Ye, Systematic evaluation of an atomic clock at 2 × 10<sup>-18</sup> total uncertainty, Nat. Commun. 6, 6896 (2015).
- [67] I. Courtillot, A. Quessada-Vial, A. Brusch, D. Kolker, G. Rovera, and P. Lemonde, *Accurate spectroscopy of Sr atoms*, Eur. Phys. J. D. 33, 161–171 (2005).
- [68] G. Jönsson, C. Levinson, A. Persson, and C.-G. Wahlström, Natural radiative lifetimes in the <sup>1</sup>P<sub>1</sub> and <sup>1</sup>F<sub>3</sub> sequences of Sr I, Z. Phys. A 316, 255–258 (1984).
- [69] H. Metcalf and P. van der Straten, *Laser Cooling and Trapping* (Springer New York, NY, 1999) pp. 50–56.
- [70] P. Morzyński, M. Bober, D. Bartoszek-Bober, J. Nawrocki, P. Krehlik, L. Śliwczyński, M. Lipinski, P. Masłowski, A. Cygan, P. Dunst, M. Garus, D. Lisak, J. Zachorowski, G. Wojciech, C. Radzewicz, R. Ciuryło, and M. Zawada, Absolute measurement of the <sup>1</sup>S<sub>0</sub> <sup>3</sup>P<sub>0</sub> clock transition in neutral <sup>88</sup>Sr over the 330 km-long stabilized fibre optic link, Sci. Rep. 5, 17495 (2015).